# Feasibility of Backcalculation Procedures Based on Dynamic FWD Response Data

WA-RD 586.1

Research Report
June 2005

Washington State
Department of Transportation

Washington State Transportation Commission
Research Office:
U.S. DOT - Federal Highway Administration

# Feasibility of Backcalculation Procedures Based on Dynamic FWD Response Data

Project Report

George Turkiyyah
University of Washington

## Abstract

The Falling weight deflectometer test (FWD) is a commonly used method for the evaluation of the structural performance of pavement systems. In the FWD test, a large weight is raised off the ground and dropped onto a rubber loading pad creating an impulse load representative of the real loading imposed by heavy traffic on the pavement. The excitation produced by the loading sets off waves in the pavement and underlying soil. Deflection time histories are gathered by an array of sensors placed at several nearby locations.

The traditional method for interpreting the FWD data to backcalculate structural pavement properties, involves extracting the peak deflection from each displacement trace of the sensors (deflection basin) and matching it through an iterative optimization method to the deflections predicted by a static model of the pavement. This approach is computationally efficient, and when the depths of the layers are known, and their properties are largely homogeneous with depth, the procedure is effective in backcalculating layer properties. However, when the depths are uncertain or when the moduli vary within a layer, the static backcalculation scheme may not yield reliable results.

The goal of this study is to investigate the feasibility and effectiveness of using the complete time history of the FWD test to overcome some of the limitations of the static backcalculation procedure, and recover pavement layer moduli distribution and thicknesses. The problem is also formulated as a numerical minimization problem, where the unknowns are the resilient moduli of thin "computational layers" that discretize the profile. Our initial findings is that this optimization formulation regularized by constraints on the magnitude and spatial gradient of the moduli, coupled with a continuation scheme for imposing the regularization terms, can overcome the ill-posedness nature of the original optimization problem. The computational effort for solving this inverse problem, however, is very significant as it requires repeated calls to the expensive forward problem: an elastodynamic simulation in stiff heterogeneous media. Additional work is needed to speed up the forward problem to be able to perform a more comprehensive evaluation with field data.

# Contents

# Chapter 1

# Introduction

## 1.1 The Problem

The Falling weight deflectometer test (FWD) is a commonly used method for the evaluation of the structural performance of pavement systems. In the FWD test, a large weight is raised off the ground and dropped onto a rubber loading pad. This creates a 20- to 70-ms impulse load with a magnitude of 10 to 260 KN. The pulse from the FWD is meant to represent a realistic loading, and the FWD test is the only commercially available system that applies loading that somewhat represents the loading that traffic imposes on the pavement.

The excitation produced by the loading sets off waves in the pavement and underlying soil. Deflection time histories are gathered by an array of sensors placed at several nearby locations (up to a distance of about 1.2 m from the point of application of the load). The response time histories are typically recorded at a high sampling rate (20-60ms).

The traditional method for interpreting the FWD data to backcalculate structural pavement properties, involves extracting the peak deflection from each displacement trace of the sensors. The peak deflections, as a function of distance, represent a deflection basin. A numerical optimization scheme is used to match this deflection basin to the deflections predicted by a model of the pavement. The optimization scheme is an iterative procedure that modifies the elastic moduli of the layers of the pavement system until a best fit is produced. Such a procedure is implemented by the WSDOT computer program, Evercalc.

This approach, using a static model and matching it to the peak deflections of the dynamic response, has several advantages. It is computationally very efficient, and when the depths of the layers are known, and their properties are largely homogeneous with depth, the procedure is effective in backcalculating layer properties. However, when the depths are uncertain or when the moduli vary within a layer, the static backcalculation scheme may not yield reliable results.

The goal of this research is to investigate the feasibility and effectiveness of using the complete time history of the FWD test to overcome some of the limitations of the static backcalculation procedure.

# Chapter 2

# Optimization-based Methods for Backcalculation with Dynamic Data

## 2.1 Idealization

The pavement model that we use in this study consists of three dimensional horizontal layers as shown in Figure 2.1.

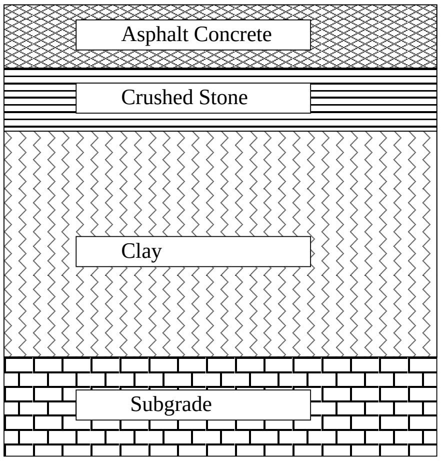

Figure 2.1: Schematic of a typical pavement profile

In WA state, it is typical practice to arrange the layers with decreasing stiffness with depth. Table 2.1 shows typical layer properties ($E$, $\nu$, $\rho$, thickness $h$) for a four layer pavement profile. The effective (resilient) modulus E (and its potential variation within a layer) and the layer depths are the primary variables to be backcalculated. We note here that some pavements have an ”inverted” profile where one of the lower supporting layers has a larger stiffness than that of one of the upper layers. The backcalculation procedures we seek to develop need not make a-priori assumptions about the profile.

Table 2.1: Mechanical properties for a typical pavement profile

| Material | E [MPa] | $\nu$ | $\rho[kg/m^3]$ | h [m] |
|---|---|---|---|---|
| Asphalt Concerte | $7.58 \cdot 10^4$ | .33 | 2100 | $0.1 - 0.2$ |
| Crushed Stone | $3.1 \cdot 10^2$ | .35 | 1900 | $0.2 - 0.4$ |
| Clay | $1.8 \cdot 10^2$ | .38 | 1900 | depending on site |
| Subgrade | $1.5 \cdot 10^2$ | .4 | 1900 | depending on site |

The specific data to be used in the backcalculation comes from the FWD response time history. Figure 2.2 shows a schematic of a FWD test. The load is applied on a loadplate which distributes it uniformly to the ground. Geophones are placed at prescribed distances from it. The actual geometrical setup varies slightly between agencies [15] but generally consists of about half a dozen geophones placed in a region of about $1.5m$ away from the loadplate. As Figure 2.2 shows, elastic waves propagate and are going to be partly reflected at the interface between two layers. The rest of the waves penetrate and propagate to the next layer where the process is repeated.

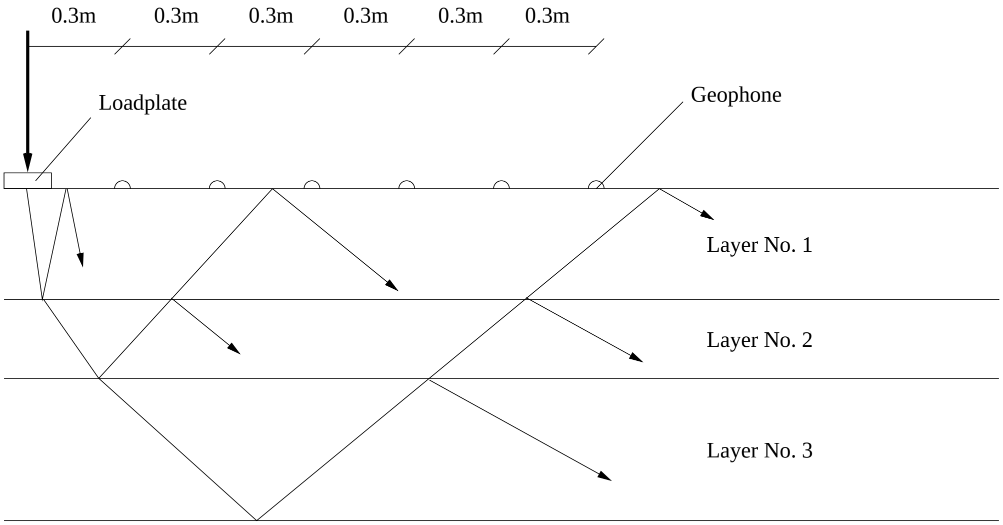

Figure 2.2: The structure of a FWD test: waves propagate and are partly reflected at layer interfaces

The simulation of the response of the system over the time scale of interest (approx. $50ms$) requires a complete elastodynamic computation and cannot be limited to a "first arrival" approach, because the waves continue either to be reflected at layer boundaries or to penetrate into other layers. So in an asphalt-concrete layer waves can—because of the high stiffness and the resulting high wavespeeds—bounce up and down a few hundred times before the complete simulation is finished. This leads to a FWD deflection which looks typically like the one shown in Figure 2.3. It can be seen that the deflection peaks occur later the further away the geophone is situated. Naturally, different configurations of subsurface layers with particular mechanical properties yield to different deflection history (peaks, shape of the response, and lag).

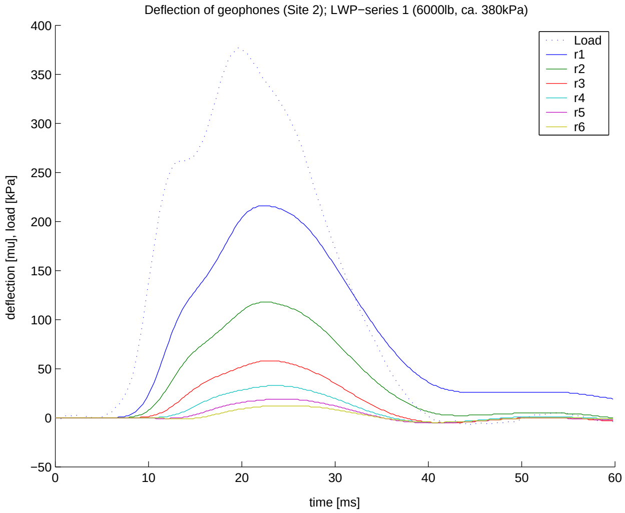

Figure 2.3: A typical FWD response: The deflection history of the geophones vs. time.

## 2.2 Basic Formulation

The formulation of an optimization problem for computing the profile of a pavement section requires three ingredients: identification of the set of unknowns to be calculated; an objective function to be optimized; and a computational strategy for finding the values of the unknowns.

In this work, the pavement section is discretized into a number of horizontal "thin layers" and the resilient moduli ($M_r$) of those layers define the set of properties to be computed by the backcalculation procedure. In order to reduce difficulties associated with roundoff arising from properties varying by many orders of magnitude between layers, it is typical to use the log of the moduli ($\mathbf{x} = \log M_r$) in the calculations. We note here that the number of computational "thin layers" do not correspond to the number of physical layers in the pavement structure. The computational layers represent a finer discretization of the depth, hence allowing for properties to vary even within a physical layer. Even though it is not strictly necessary, we assume constant properties within a computational layer.

The objective function to be minimized is the difference between the recorded response at the receivers and the computed response of a pavement profile whose properties are encoded in the vector $\mathbf{x}$. This represents the error in the model, and the minimization problem may be written as:

$$\min_{\mathbf{x}\in\Re^n} E(\mathbf{x}) = \|\boldsymbol{f}(\boldsymbol{x})\|_2^2 = \sum_{i=1}^{nr}\sum_{j=1}^{nt} ||f_{\text{rec}}(i,j) - f_{\text{com}}(i,j,\mathbf{x})||^2 \qquad (2.2.1)$$

where $n$ is the number of computational layers, $nr$ is the number of receivers, $nt$ is the number of time steps in the recorded response, and $f_{\text{rec}}$ and $f_{\text{com}}$ are the recorded and computed motions respectively.

Since this error function is continuous with respect to $\mathbf{x}$, gradient-based methods are the preferred numerical methods for computing the minimum. These methods require the repeated evaluation of the error (objective) function and its derivatives. The evaluation of the objective function for a given pavement profile ($\mathbf{x}$), involves performing an elastodynamic simulation in order to compute the function $f_{\text{com}}$. This is known as a "forward solution" and is the most computationally expensive portion of the computation, and will be discussed in the next chapter. The computation of the derivatives is best performed using an adjoint method which, from a computational view, involves an additional evaluation of the objective/error function.

## 2.3 Regularization Schemes

Unfortunately, a straightforward numerical optimization to minimize the error function above generally fails. The mathematical problem is not well-posed in the sense that small perturbations in the input, can lead to very different results. In order to be able to robustly obtain a meaningful set of parameters, the minimization problem is replaced by a related one that has improved numerical properties. This is known as *regularization*.

### 2.3.1 Regularization Parameters

Regularization is one technique used to solve ill-posed problems. Mathematically, regularization involves redefining Eq. 2.2.1 as:

$$\min_{x \in \Re^n} F(\boldsymbol{x}) = E(\boldsymbol{x}) + \|\boldsymbol{\Omega}(\boldsymbol{x})\|_2^2 \tag{2.3.1}$$

The original least-squares error term, or *residual norm*, has been regularized by a *side constraint*, $\|\boldsymbol{\Omega}(\boldsymbol{x})\|_2^2$.

One side constraint commonly used is:

$$\|\boldsymbol{\Omega}(\boldsymbol{x})\|_2^2 = \lambda^2 \|\boldsymbol{L}\boldsymbol{x}\|_2^2. \tag{2.3.2}$$

where $\lambda$ is a regularization parameter, and $\boldsymbol{L}$ for present purposes, will be taken as an $n \times n$ identity matrix, $I$. $\lambda$ controls the weight of the regularization term. A large $\lambda$ desensitizes the residual term and forces a minimum to occur at a low value of $x$, while at small $\lambda$, the side constraint disappears [8].

Physically, the side constraint changes $F$ by adding a quadratic surface to the residual norm. This stabilizes the optimization process by sliding each step toward the true minima. Fig. 2.4 illustrates this for a univariate objective function. Choosing a proper value of $\lambda$ is important to achieve the correct amount of regularization. A large $\lambda$ will move optimization away from the true minima, while a small $\lambda$ may not be effective in regularizing the function. The contour plots in Fig. 2.5 show the effect of various values of the regularization parameter on a two-variable objective function.

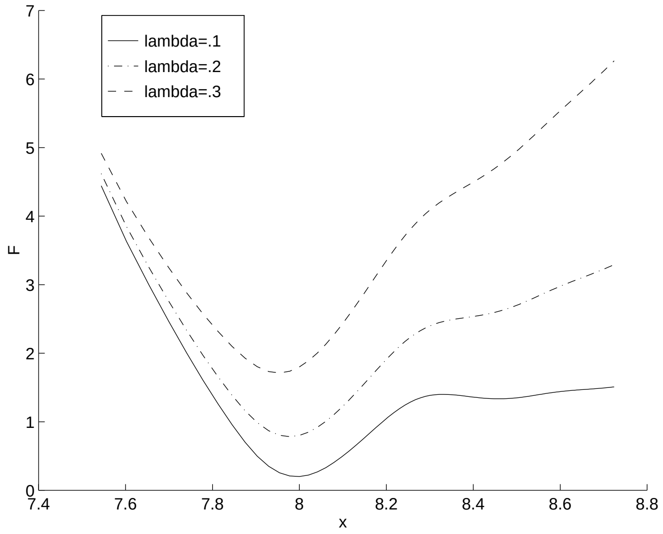

Figure 2.4: Regularized 1D Function

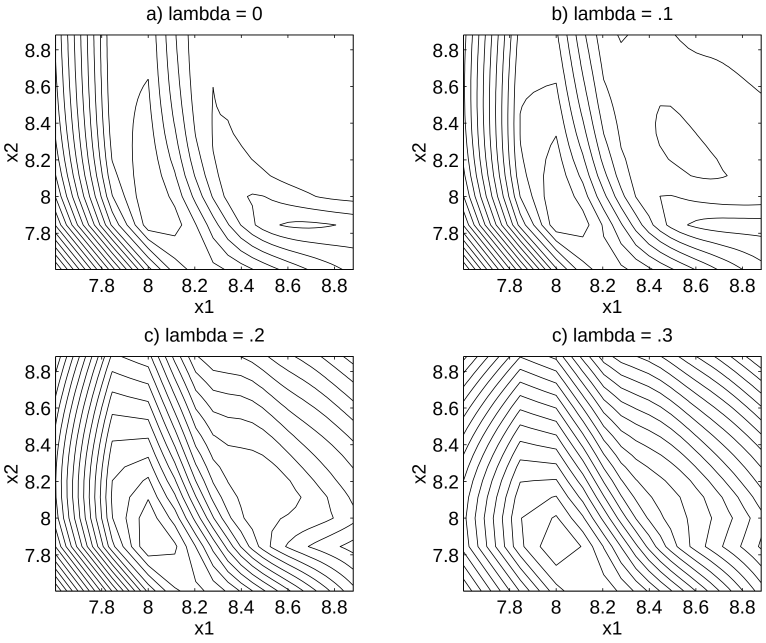

Figure 2.5: Contour Plots of Regularized 2D Function

Regularization is generally used when solving ill-posed least squares problems. A plot that is often used to describe the influence of $\lambda$ is called an *L-curve* [9] (Fig. 2.6). L-curves are plots that illustrate solutions to a regularized linear least squares problem at different values of $\lambda$. The curve is a log-log plot of the solution, where the x-axis represents residual norm values (2.2.1) and the y-axis represents the regularizing side-constraint (2.3.2) values. A larger $\lambda$ induces more regularization or "filtering". Effects of smaller $\lambda$, or less filtering may be noted, as one moves along the L-curve.

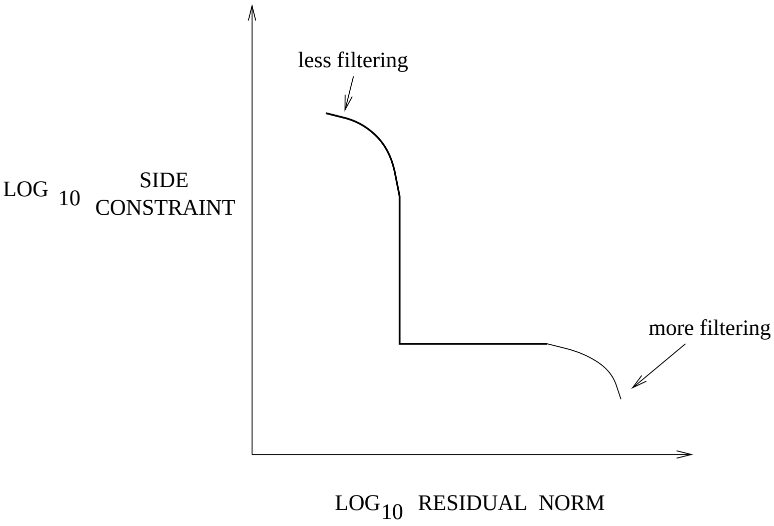

Figure 2.6: L-curve

### 2.3.2 Regularization of FWD Backcalculation

As mentioned above, minimization of the error residual does not guarantee convergence. Using initial moduli values for the iterative optimization procedure ($\boldsymbol{x}_{seed}$) close to the solution may end with a correct result. However, a start farther away from the solution may not. Even when $F$ is a function of one parameter (Fig. 2.4), a gradient based optimization algorithm with a high starting point ($x > 8.3$) will result in a diverging solution if the unregularized error is minimized.

Regularization alters the function surface by adding a parabolic characteristic to $F$ that prevents divergent solutions. To evaluate the effect of a regularization term on FWD data, we consider the following form for $F$

$$F = E(x) + \lambda^2 \| \frac{\boldsymbol{x} - \boldsymbol{x}^o}{length(\boldsymbol{x})} \|_2^2, \tag{2.3.3}$$

where a side constraint, $\| \frac{\boldsymbol{x} - \boldsymbol{x}^o}{length(\boldsymbol{x})} \|_2^2$ has been added, and $\lambda$ weighs this new term. The denominator for this new term was added as a form of normalizing the regularization term, making it independent to the number of layers in the pavement. Equation 2.3.3 is a nonlinear version of Tikhonov Regularization in standard form [8].

An illustration of regularization effects is shown in Figure 2.7. Figure 2.7 illustrates the reconstruction of a uniform profile, using different values of the parameter $\lambda$. The horizontal axis shows the $\lambda$ values and the vertical axis shows the reconstructed profile which has been discretized using 20 thin computational layers. Each run in Figure 2.7 has $\boldsymbol{x}_{seed} = 8 \times ones(20, 1)$ and $\boldsymbol{x}^o = 7 \times ones(20, 1)$, but uses a different value of $\lambda$ ($2^{15}$ to $2^{-9}$, exponentially decreasing by two). The upper left corner plot illustrates how optimization converges to a minimized side constraint solution ($\boldsymbol{x}^* = 7 \times ones(20, 1)$) at a large value of $\lambda$, and slowly converges to the minimized residual norm solution ($\boldsymbol{x}^* = 8 \times ones(20, 1)$) as $\lambda$ decreases. The lower left plot illustrates this relationship in terms of the actual objective function, residual norm, and side constraint values.

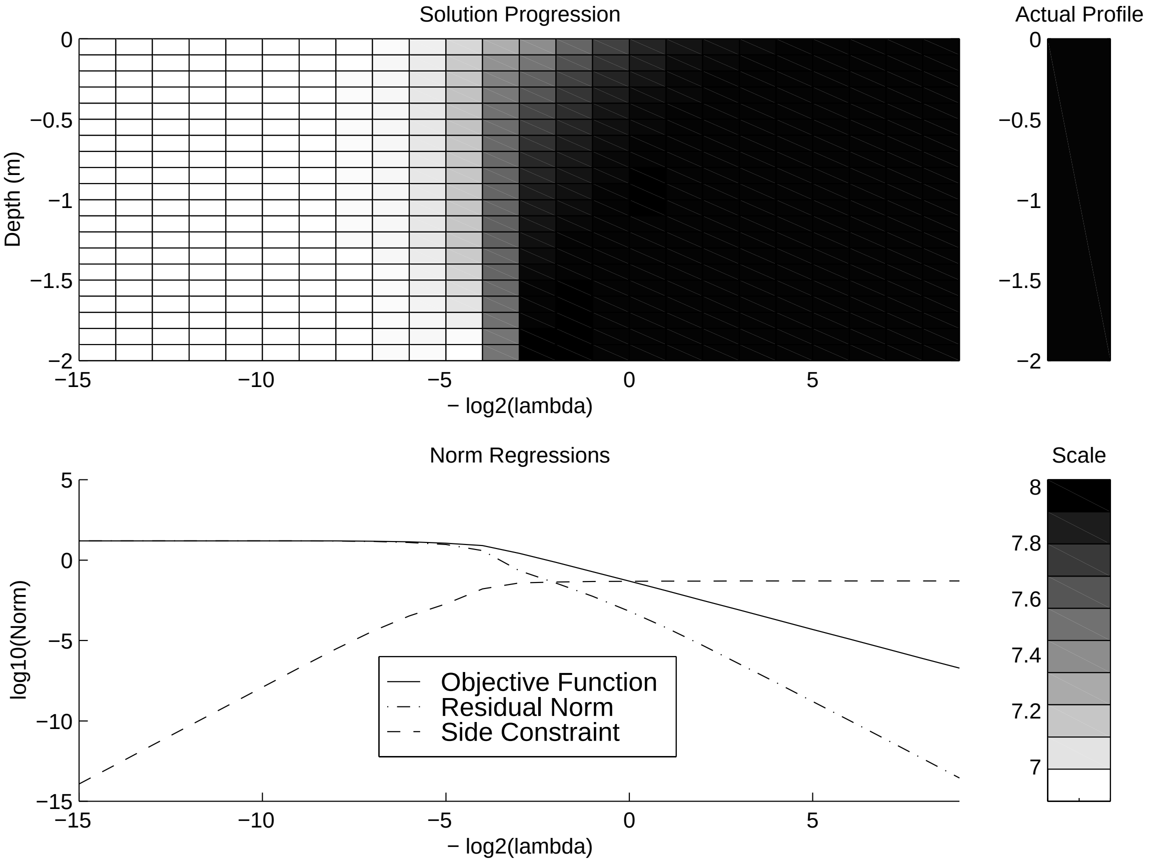

Figure 2.7: Regularization Results-Stiffness Values

A better comparison of the norm values may be illustrated by plotting $log_{10}\|\boldsymbol{x} - \boldsymbol{x}_o\|_2^2$ ($log_{10}$ of the side constraint) vs $log_{10}\|\boldsymbol{f}(\boldsymbol{x})\|_2^2$ ($log_{10}$ of the residual norm) for each run (Fig. 2.8). Each asterisk corresponds to a solution for one value of $\lambda$. For a run with a large value of $\lambda$, $\lambda > 2^5$, the solution is insensitive to the residual norm value, and highly sensitive to the side constraint, resulting in the vertical line depicted. As $\lambda \rightarrow 1$, a behavior reversal can be observed, and as $\lambda \rightarrow 0$, the side constraint value levels off, minimizing the residual norm.

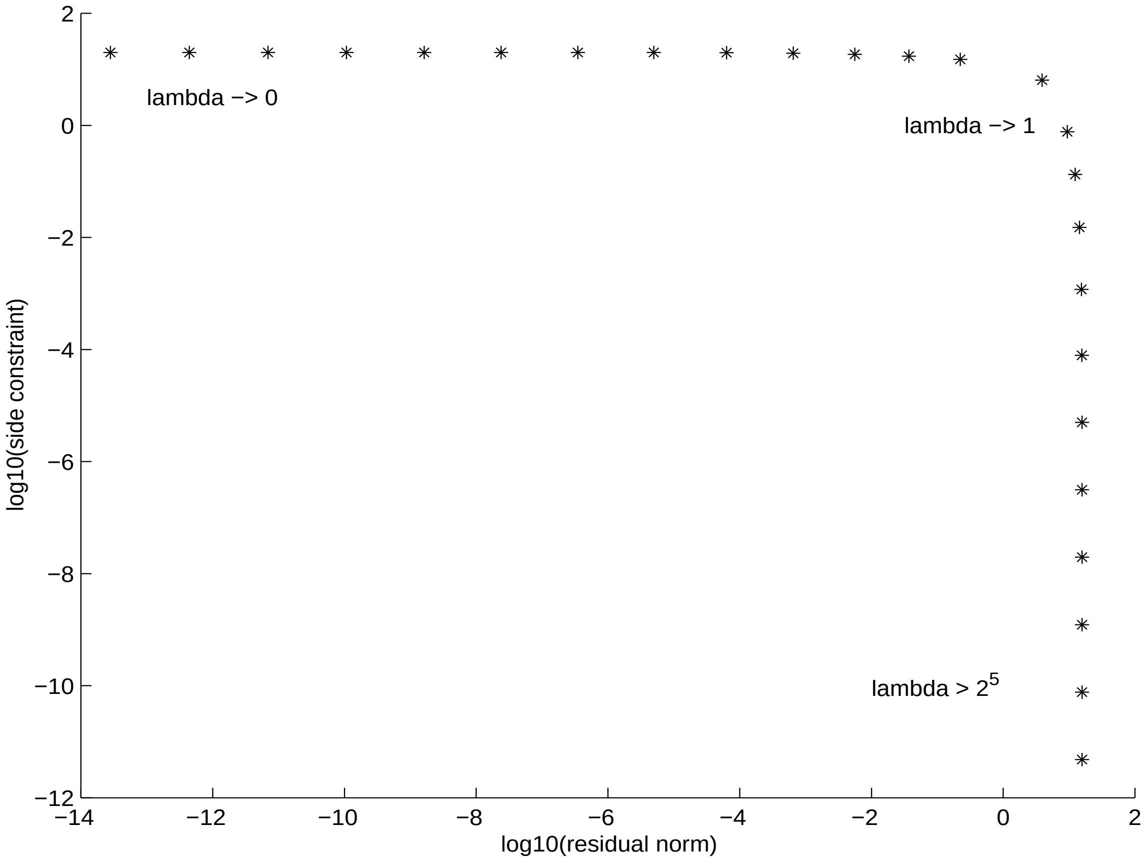

Figure 2.8: Regularization Results-Norm Values

### 2.3.3 Difficulties of a-priori Choice of Parameters

Figures 2.7 and 2.8 illustrate convergence under ideal conditions since a seed value of $\boldsymbol{x}_{seed} = 8 \times ones(20,1)$, the solution profile, was used. Figures 2.9 and 2.10 depict results for the same strategies used to produce Figures 2.7 and 2.8, except $\boldsymbol{x}_{seed} = 11 \times ones(20,1)$ was used. Figures 2.9 and 2.10 illustrate increasing instability at lower $\lambda$ values. Solutions with $\lambda = \frac{1}{2}, \frac{1}{4}, 2^{-3}, \ldots$ were divergent and not useful as backcalculation results. The profile obtained through minimization of the objective function shows a soft top layer, a very stiff middle region, and a soft bottom layer! Such solutions are not physically meaningful.

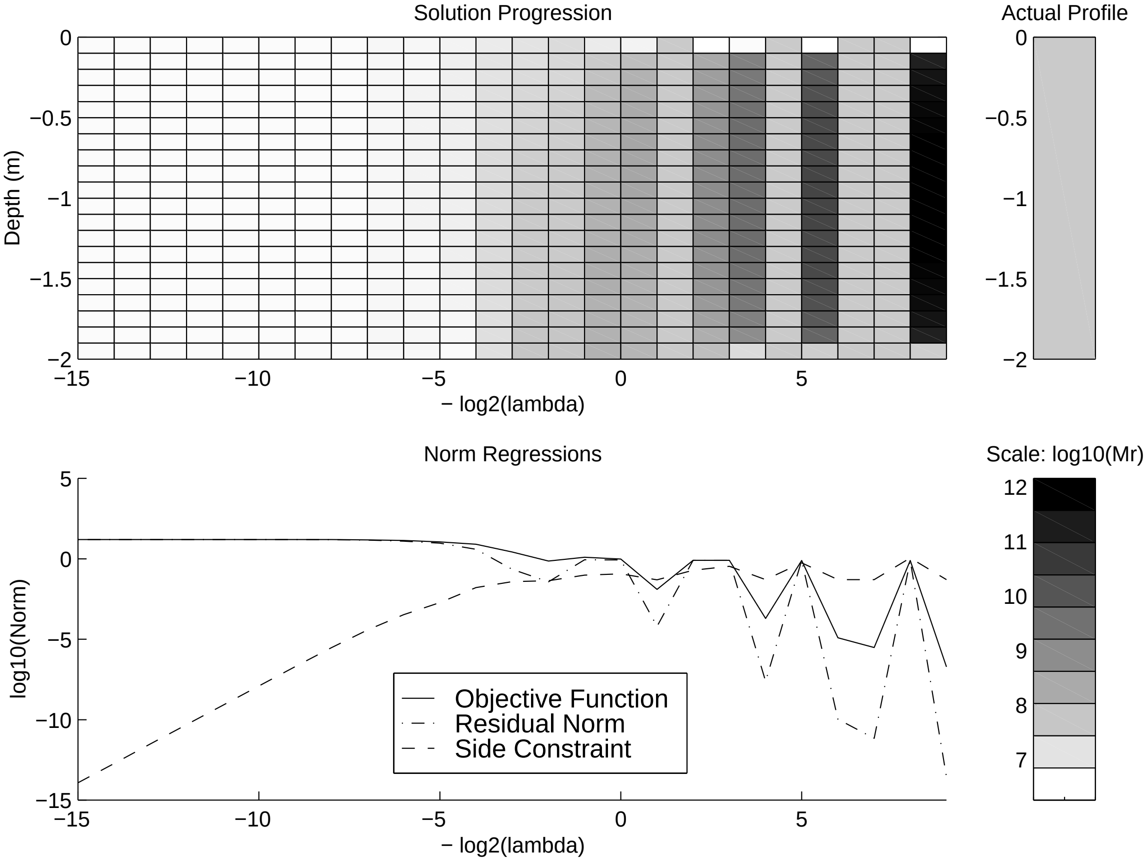

Figure 2.9: Justifying Continuation-Stiffness Values

The examples above illustrate a general trend: small values of $\lambda$ do not regularize the solution sufficiently and result in divergent solutions; large values of $\lambda$ change the minimization function significantly and do not converge to the true solution. In essence, large values of $\lambda$ "smooth" the objective function at the expense of shifting the true minimum. Small values, on the other hand, do not sufficiently smooth the objective function and a gradient-based numerical optimization gets "stuck" in a local, not physically meaningful, minimum, or does not converge at all. It is therefore essential to choose appropriate values of $\lambda$ for the optimization procedure, to balance these two competing demands.

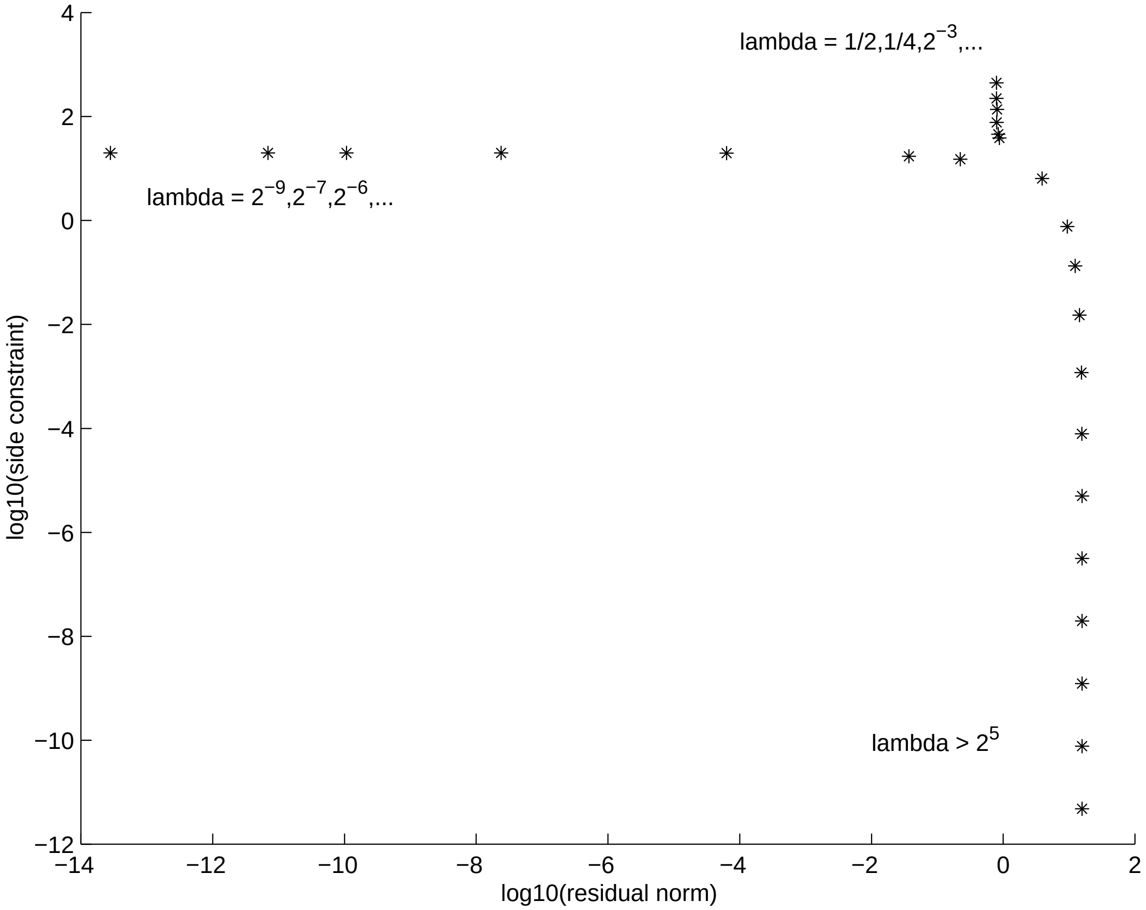

Figure 2.10: Justifying Continuation-Norm Values

Unfortunately, it generally not possible to do so a-priori. The choice of the proper regularization parameter depends on the specific nature of the pavement profile, relative stiffness values, and has to be determined at run-time. A strategy for adaptively discovering the proper value consists of starting with a large $\lambda$ (giving a smooth but modified objective), performing an optimization, and using the converged solution as the starting point of another optimization problem with a smaller value of $\lambda$. Incorporating such a strategy is known as a *continuation* approach, and has been used in the past [5] for adaptive regularization.

### 2.3.4 Continuation Methods for Adpative Regularization

To illustrate the ability of a continuation method of avoiding non-physical solutions, we considered the same uniform profile above, with a starting value of $\boldsymbol{x}_{seed} = 11 \times ones(20,1)$, which should be higher than any moduli expected ($M_r < 10^{11}$ Pa), and an initial side constraint constant of $\boldsymbol{x}_o = zeros(20,1)$. Each optimization call was limited to $length(\boldsymbol{x})$ steps, an "efficient" amount of allowed optimization iterations (after that, the objective function decreased very slowly). Choosing these values represented a start without any a priori knowledge of the pavement profile. Figure 2.11 illustrates results from this continuation strategy. As expected, by reducing $\lambda$ slowly, the divergent solutions present in Figures 2.9 have been eliminated.

## 2.4 Effect of Noise

Instrumentation error exists in all field data. In order to assess the effect of noisy data, a random perturbation was added to the synthesized data used in the previous examples. Using the continuation strategy described above and synthesized deflection noise of $\epsilon(5\%)$ did not result in convergence to a smooth solution. Figure 2.12 illustrates the continuation run utilizing noisy data. $\boldsymbol{x}^* = \{8.169, 7.765, 7.795, 8.179, 8.355, 8.313, 8.137, 8.010, 8.091, 8.015, 7.768, 7.687, 7.856, 8.026, 8.145, 8.229, 8.289, 8.269, 8.084, 7.770\}$ ($\boldsymbol{x} = log_{10}(M_r)$). The solution differs from the actual profile by having alternating stiff and soft layers. Such solutions are known as *rough.* Objective function and residual norm values do not decrease to the same extent as the corresponding values do in Figure 2.11.

These solutions are only likely to worsen when more complex pavement profiles are reconstructed. Rough solutions are generally a product of noisy data that alters the error function surface enough to lead optimization astray. To prevent this behavior, a second side constraint that controls roughness was added to $F$:

$$F = E(x) + \lambda^2 \| \frac{\boldsymbol{x} - \boldsymbol{x}^o}{length(\boldsymbol{x})} \|_2^2 + \lambda^2 \| \boldsymbol{x}_{top} - \boldsymbol{x}_{bottom} \|_2^2, \tag{2.4.1}$$

with $\boldsymbol{x}_{bottom} = (log_{10}(M_{r,1}), \ldots, log_{10}(M_{r,i-1}))^T$, $\boldsymbol{x}_{top} = (log_{10}(M_{r,2}), \ldots, log_{10}(M_{r,i}))^T)$, for a pavement with $i$ elements. This second side constraint, sometimes called a *smoothness penalty,* controls stiffness changes between adjoining elements, preventing roughness. A solution that utilizes this second smoothing term converged to $\boldsymbol{x} = \{7.985, 7.986, 7.988, 7.990, 7.992, 7.994, 7.996, 7.997, 7.998, 7.999,$

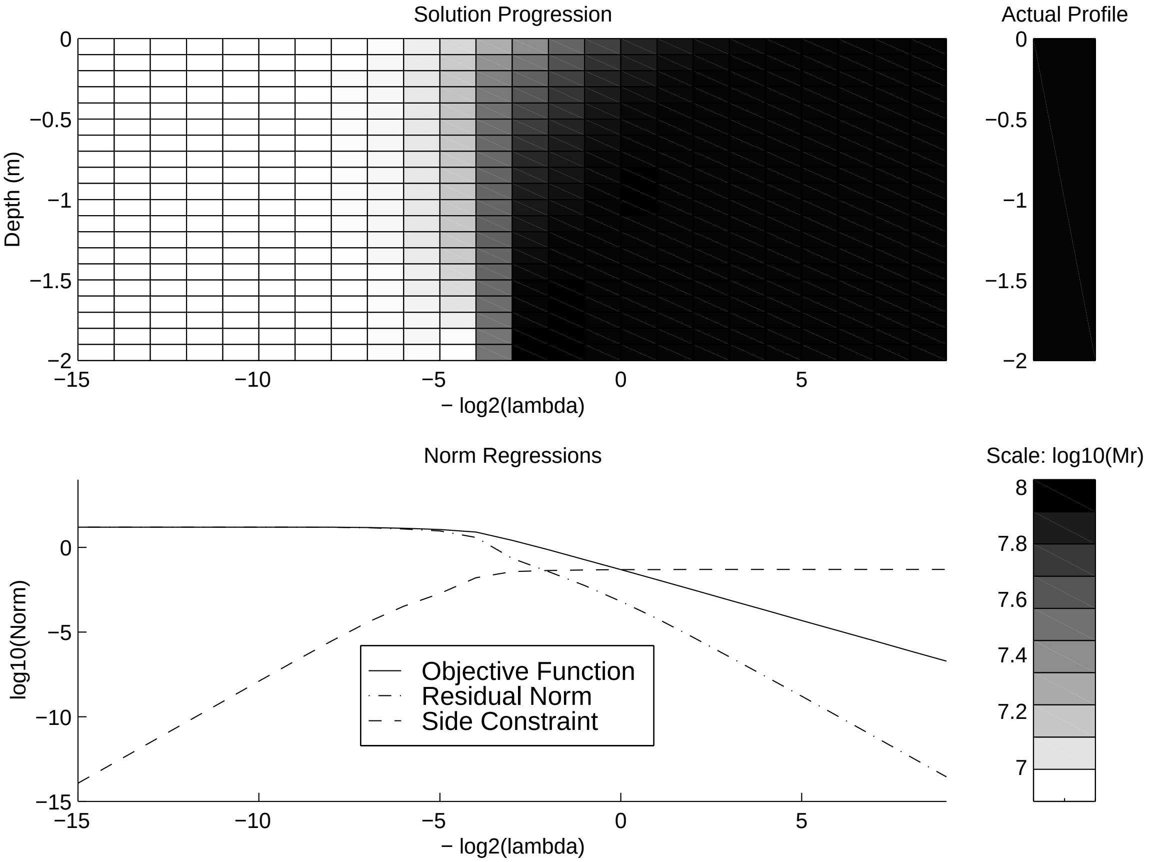

Figure 2.11: Continuation Results-Stiffness Values

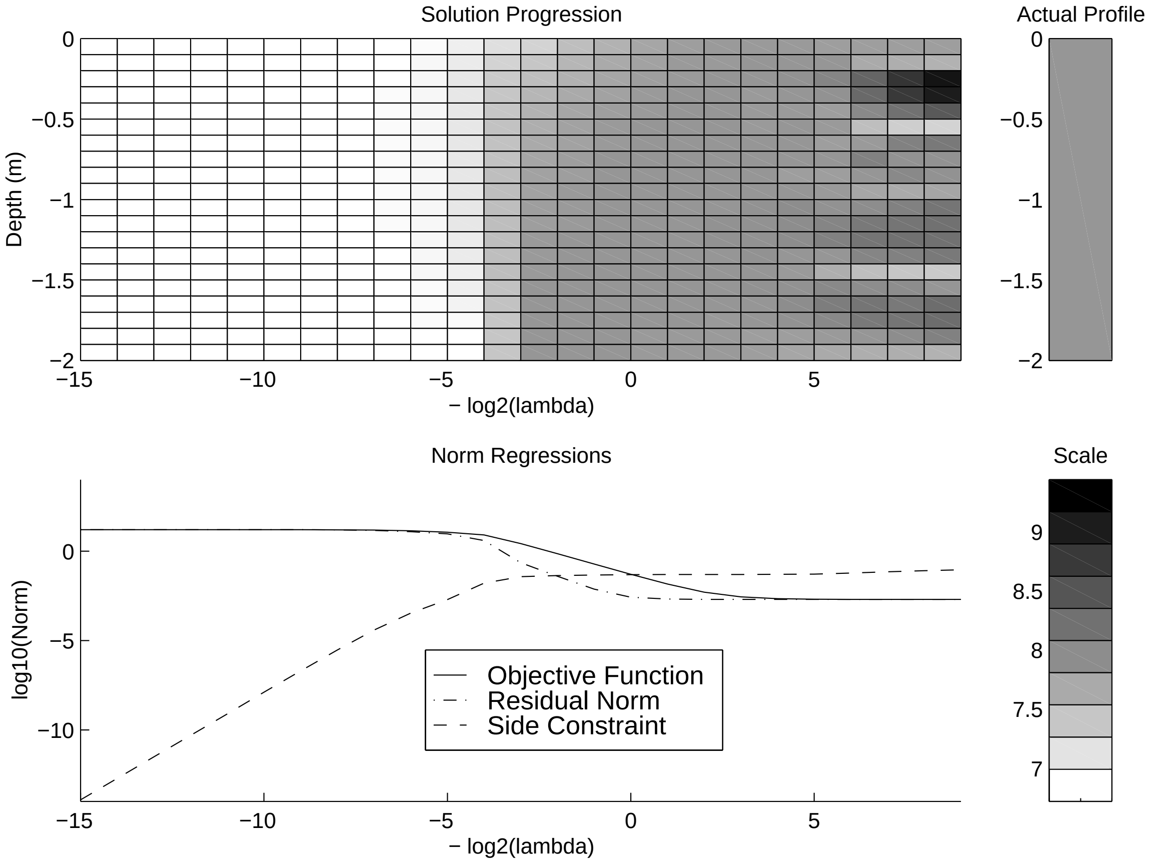

Figure 2.12: Rough Results-Stiffness Values

$7.999, 7.999,\ 7.999, 7.999, 8.000, 8.000, 8.000, 8.000, 8.000, 8.000\}$.

The results of adding a smoothing penalty term are illustrated in Figure 2.13, with a log-log plots of the second side constraint and residual norm in Figure 2.14. Figure 2.14 has features of Hansen's L-curve, Figure 2.6. At large $\lambda$, the vertical trend is again present, then as $\lambda \rightarrow 4$, leveling off occurs; when $\lambda < 4$ a different behavior can be noted. Both the residual norm and smoothness term decrease (marked by the o's in Figure 2.14). This behavior is favorable because the profile becomes smoother and more accurate simultaneously, A solution at $\lambda = \frac{1}{2}$, or the "corner" of this plot, represents the closest result to the actual profile: $\boldsymbol{x} = \{7.985, 7.986, 7.988, 7.990, 7.992, 7.994, 7.996, 7.997, 7.998, 7.999, 7.999, 7.999, 7.999, 7.999, 8.000,$
$8.000, 8.000, 8.000, 8.000, 8.000\}$ After passing this corner ($\lambda < \frac{1}{2}$), roughness increases, marked by the rising smoothing penalty norm. The corner of the curve is the ideal solution.

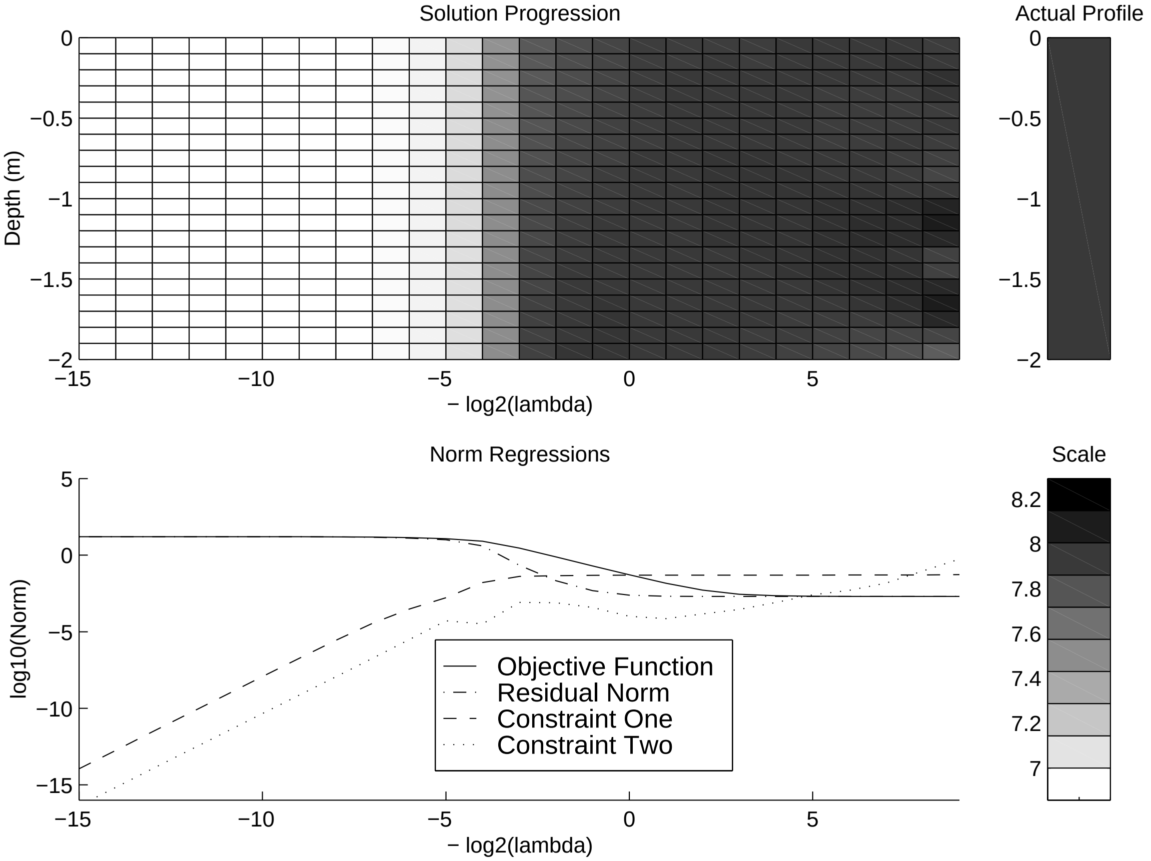

Figure 2.13: Results With Second Side Constraint-Stiffness Values

A more effective continuation approach also resets the side constraint constant, $\boldsymbol{x}^o$, to the solution of the previous call. This addition alters the objective function by moving the parabolic regularization surface to a more effective spot for optimization, and it also relinquishes the responsibility of defining a value for $\boldsymbol{x}^o$ at each optimization call. Corresponding plots of this extended continuation approach are illustrated in Figures 2.15, 2.16, and 2.17, with $\boldsymbol{x}^o = zeros(20, 1)$ and initial seed parameters,

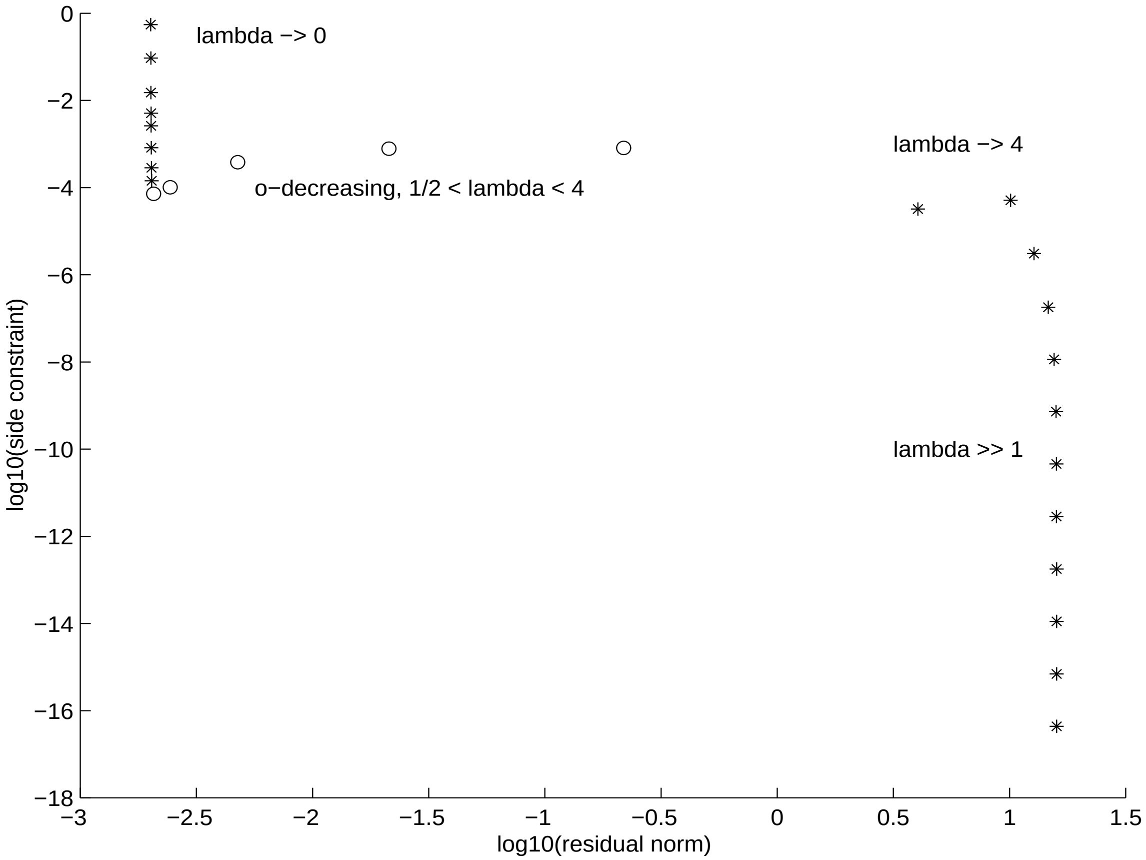

Figure 2.14: Results With Second Side-Constraint, Second Side-Constraint Values

$\boldsymbol{x}_{seed} = 11 \times ones(20, 1)$.

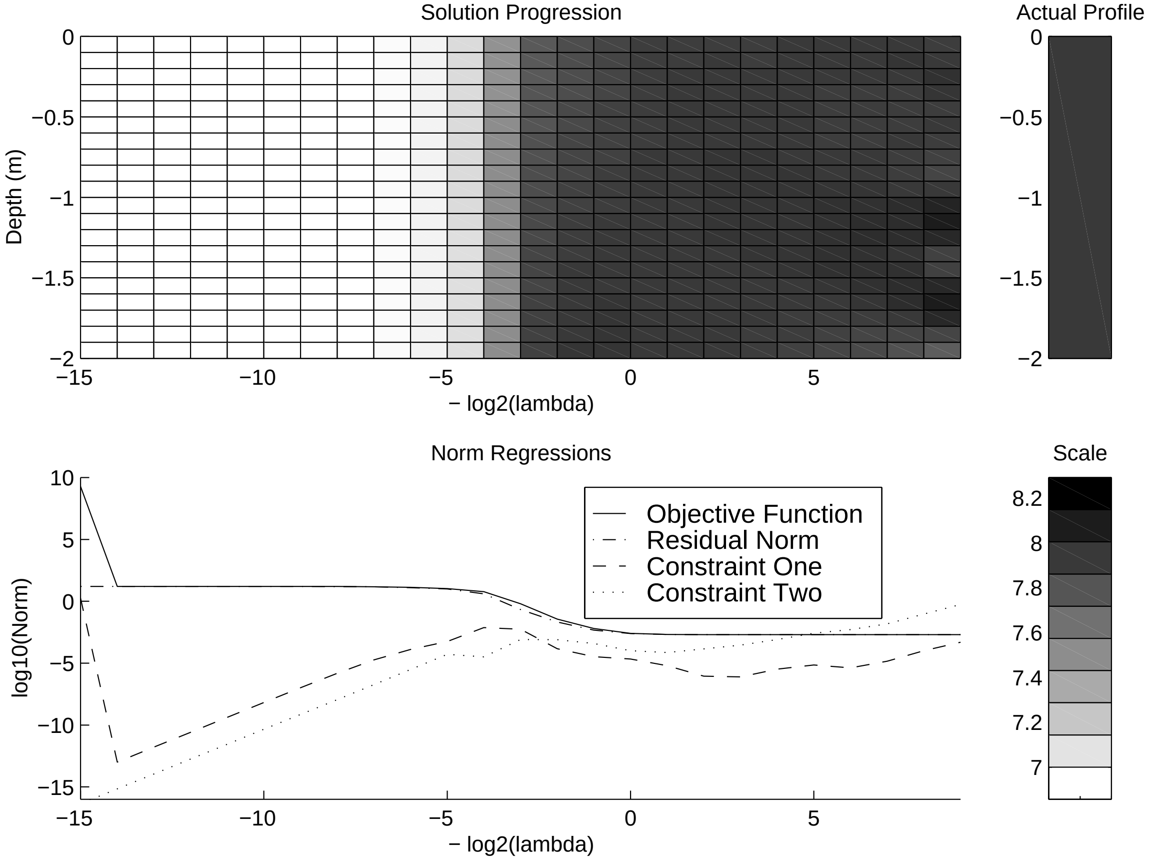

Figure 2.15: Additional Continuation, Stiffness Values

With this change, both side constraints behave in a similar manner with an increasing side constraint at large $\lambda$, a negative gradient as $\lambda \rightarrow 1$ (marked by o's) in Figures 2.16 and 2.17, then an increasing side constraint as $\lambda \rightarrow 0$. Again, at the corner ($\lambda = \frac{1}{2}$), convergence to the correct solution occurs.

## 2.5 Examples

In this section, the regularized optimization problem with a continuation method is tested on a number of backcalculation problems. The results are from synthetically generated data with random noise both in 1D and 3D, and from field data. The one dimensional problem (which assumes that pavement behavior may be approximated by a one-dimensional vertical equivalent) was used in testing to speed up the development, since the three dimensional problem formulation requires an expensive elastodynamic simulation (forward solution) at every optimization iteration. In the next chapter we will describe methods we developed for efficient 3D forward simulations.

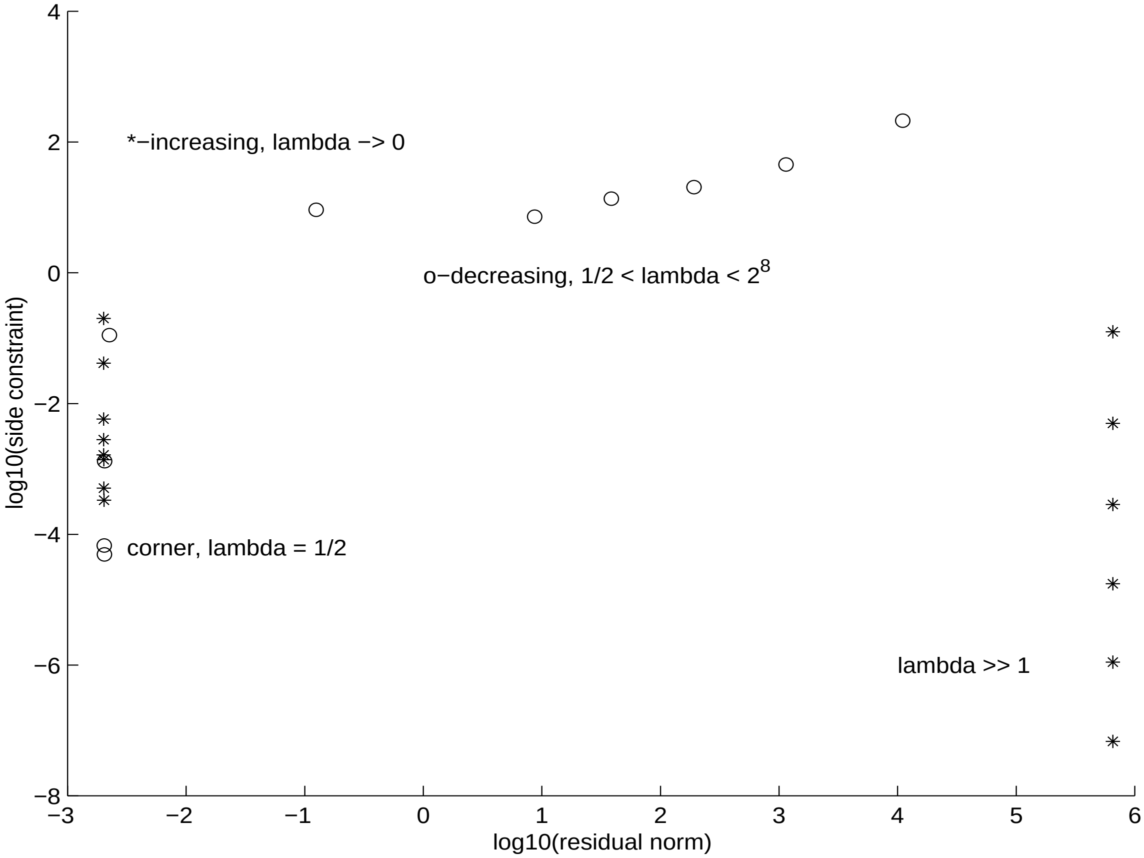

Figure 2.16: Additional Continuation, First Side-Constraint Values

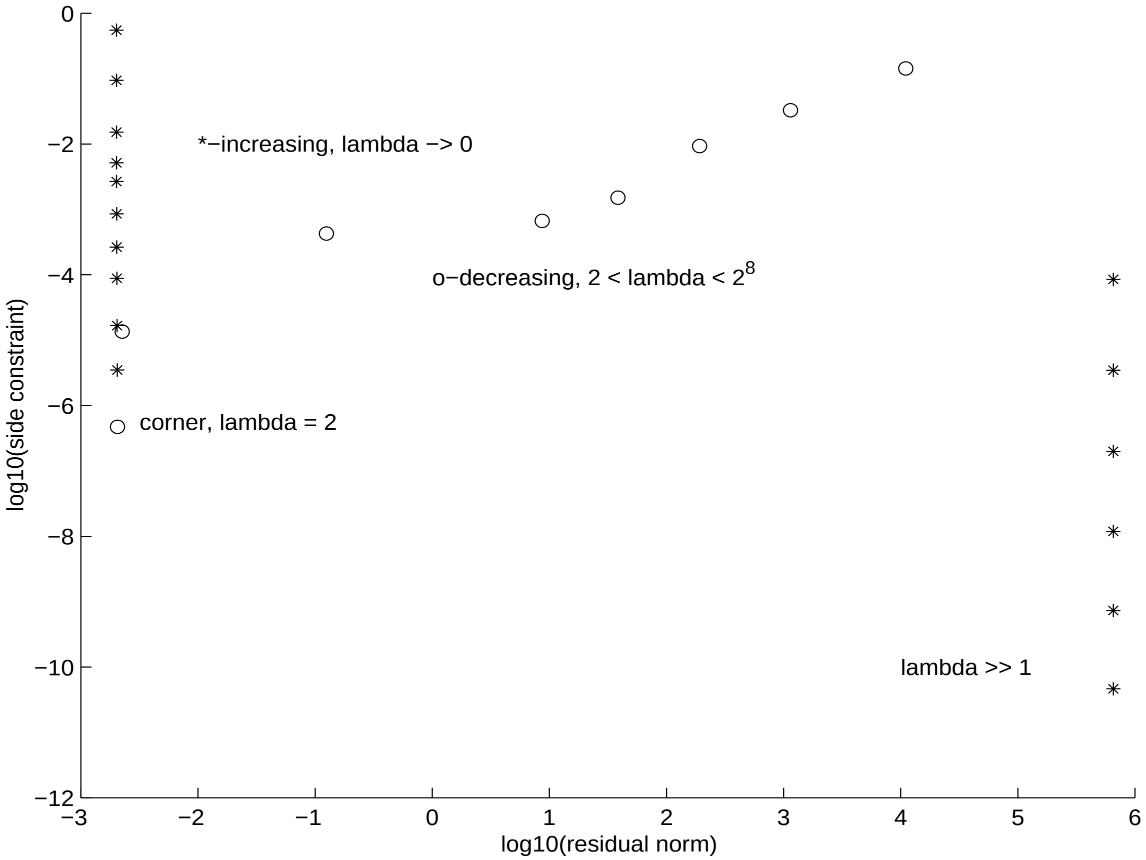

Figure 2.17: Additional Continuation, Second Side-Constraint Values

In the computations, we use a Levenberg-Marquardt method with a quadratic polynomial line-search for the solutions of the nonlinear least squares subproblems. An initial value of $\lambda$ was chosen to ensure that the side constraints will be larger than the residual norm and that a high seed value will decrease to the correct magnitude. $\lambda$ was decreased according to the value of the residual $E(x)$ after each optimization solution. Once the rate of decrease of the residual norm had slowed down (the solution began to get rougher), the algorithm stopped. That solution was taken as the backcalculated profile.

The results are presented in the following form. The actual profile (that was used to generate the synthetic data for the backcalculation) is shown on the upper right. For problems using field data, the best available estimate of the profile is shown. The progress of the optimization procedure is shown along a horizontal axis. The axis shows the number of least squares iterations. On the vertical axis, the evolving backcalculated profile is shown. On the left is the initial profile (grayscale map) which changes to the final converged profile on the right. The lower left plot shows the corresponding decrease in the objective function during the backcalculation.

### 2.5.1 One dimensional Problems

Figure 2.18 illustrates a run for a three layered pavement system. The profile is discretized into twenty computational layers with one variable per layer. Physical layer thicknesses may be readily obtained from these results.

Another set of runs compared the results between two systems with similar static stiffnesses. Backcalculation of these profiles is difficult to achieve using a static deflection basin based strategy. Figure 2.19 illustrates backcalculation of a system with a $.2\ m$ top layer moduli of $10^9\ Pa$. Figure 2.20 illustrates backcalculation of a system with a top layer with doubled stiffness, $2 \times 10^9\ Pa$, and thickness, $.4\ m$ (same static stiffness). Using the time history based backcalculation strategy resulted in correct convergence for both cases.

### 2.5.2 Three-dimensional Problems

Figure 2.22 shows the results from a 3-layer profile reconstructed using a three-dimensional forward problem. The data used is shown in the reconstruction is shown in Figure 2.21. The system was discretized into 10 computational layers, and had a uniform starting profile (the first iterations in each run were cut off to better illustrate the contrasting shaded layers). After about eighty least square iterations, the profile results converged to the actual profile. Continuation influences may be observed by studying objective function values. Sudden drops indicated breaks between optimization calls, where a new regularization ($\lambda$) value was being used. Actual moduli: $1e9 \times ones(4,1); 5e8; 5e8; 1e8 \times ones(4,1)$ (250 mm top layer, 250 mm middle layer, 1.5 m bottom layer) were compared to the final backcalculated moduli: $\{1.000e9, 9.999e8, 1.000e9, 9.999e8, 5.000e8, 5.000e8, 1.000e8,\ 1.000e8,\ 1.000e8,\ 1.000e8\}$ to illustrate correct convergence. (All stiffnesses are in Pascals).

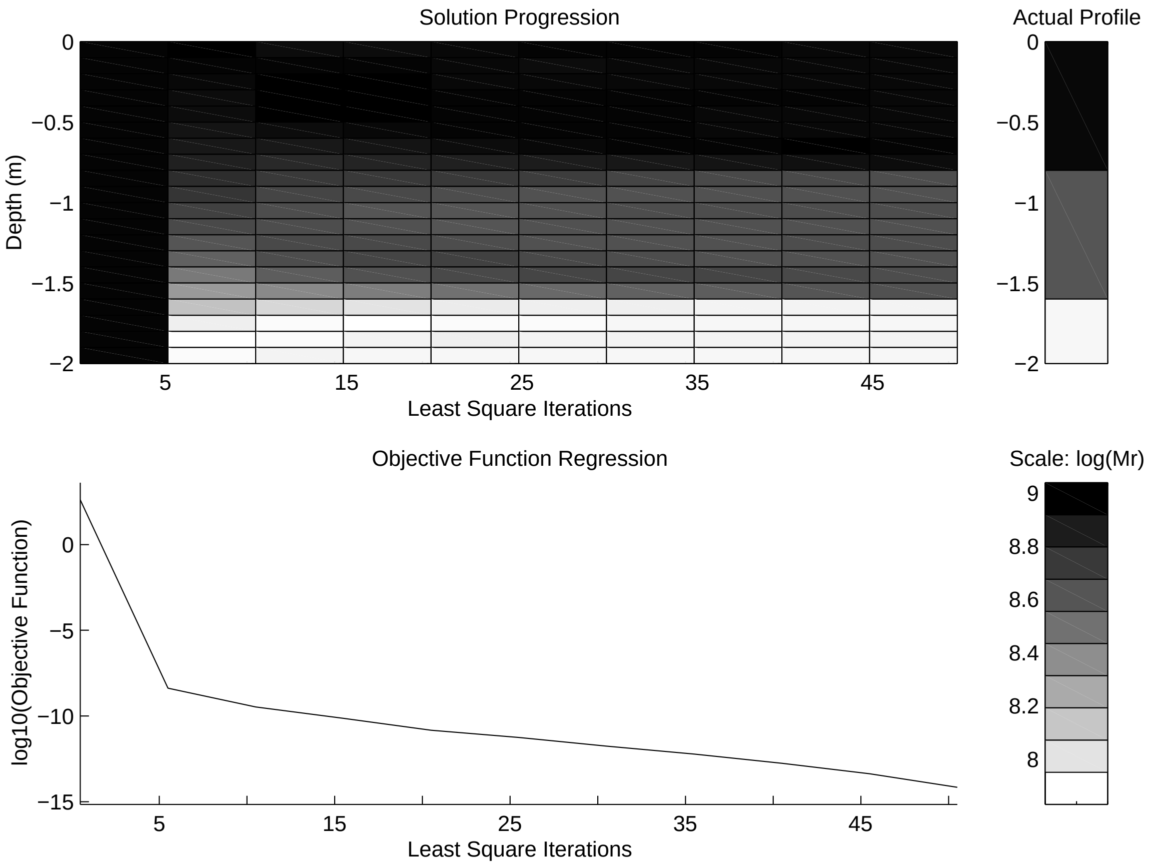
Solution Progression

Actual Profile

Objective Function Regression

Scale: log(Mr)

Figure 2.18: One-Dimensional Backcalculation Run-Multiple Layers

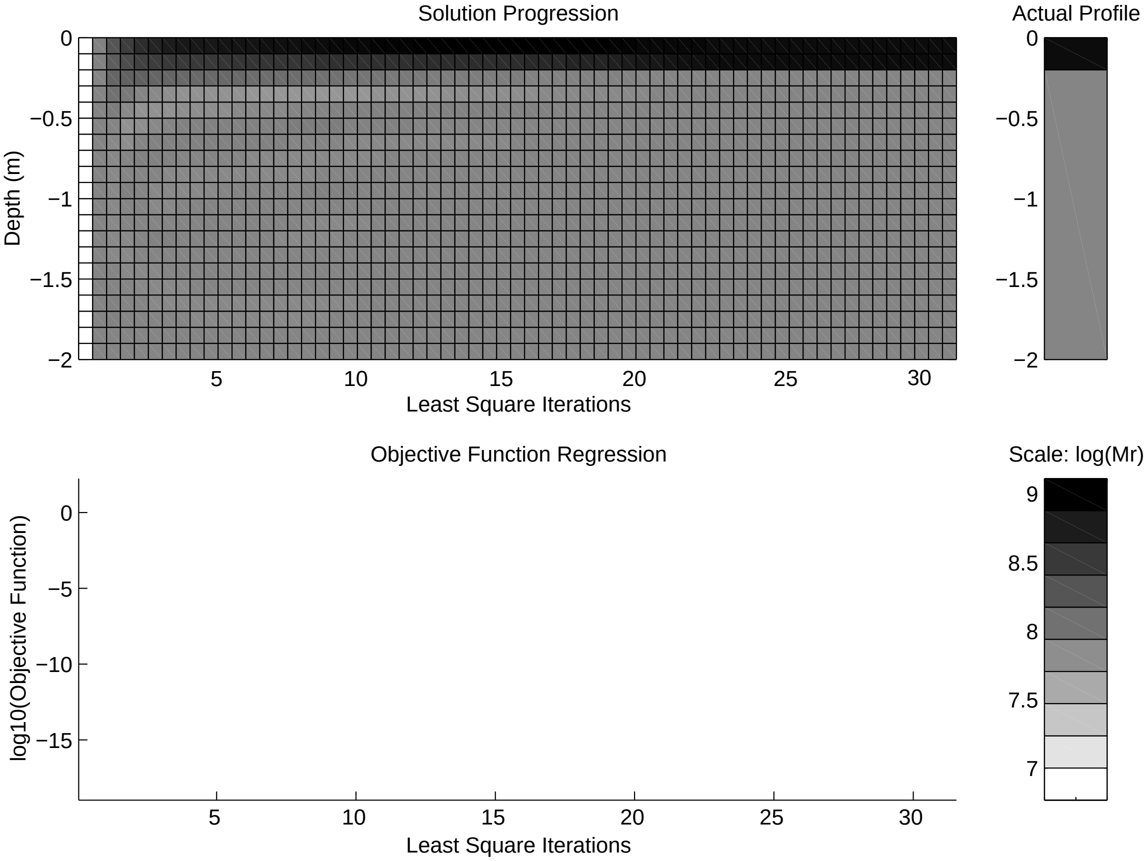

Figure 2.19: One-Dimensional Backcalculation Run-Soft/Thin Surface

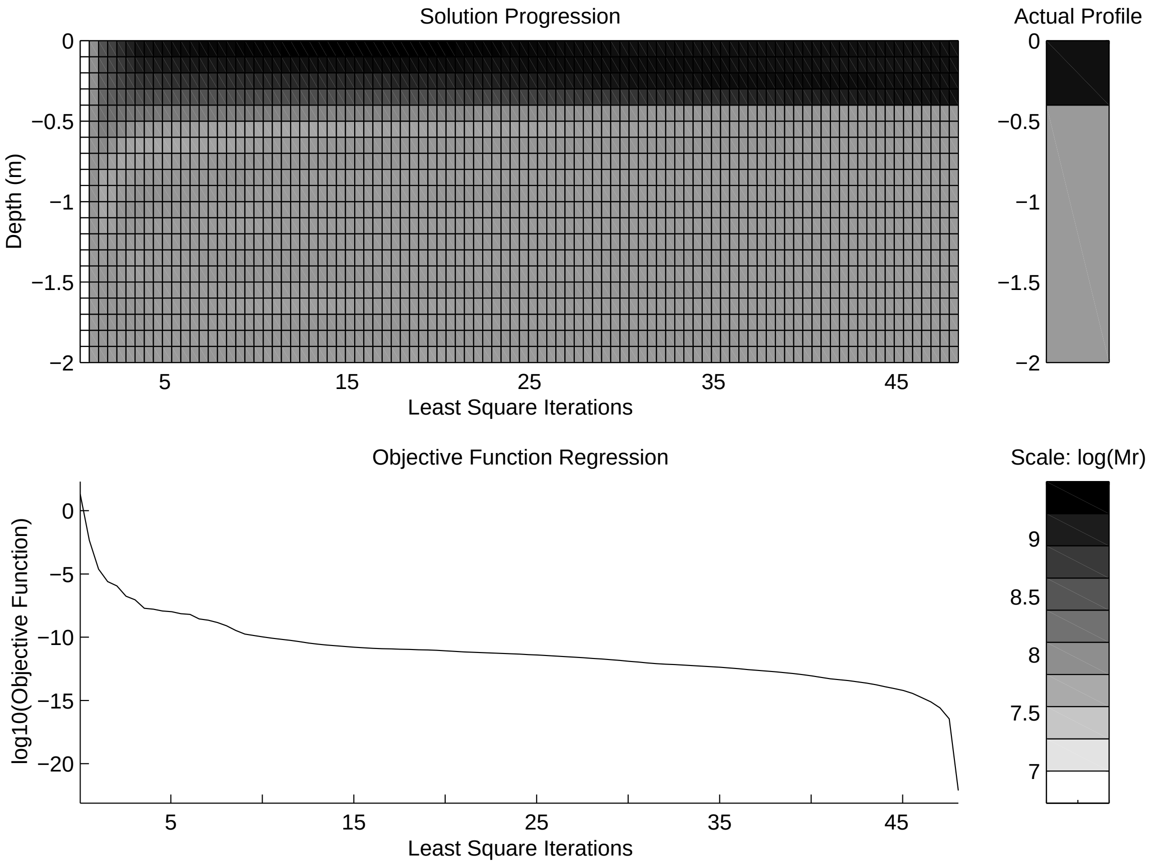
Solution Progression

Actual Profile

Objective Function Regression

Scale: log(Mr)

Figure 2.20: One-Dimensional Backcalculation Run-Stiff/Thick Surface

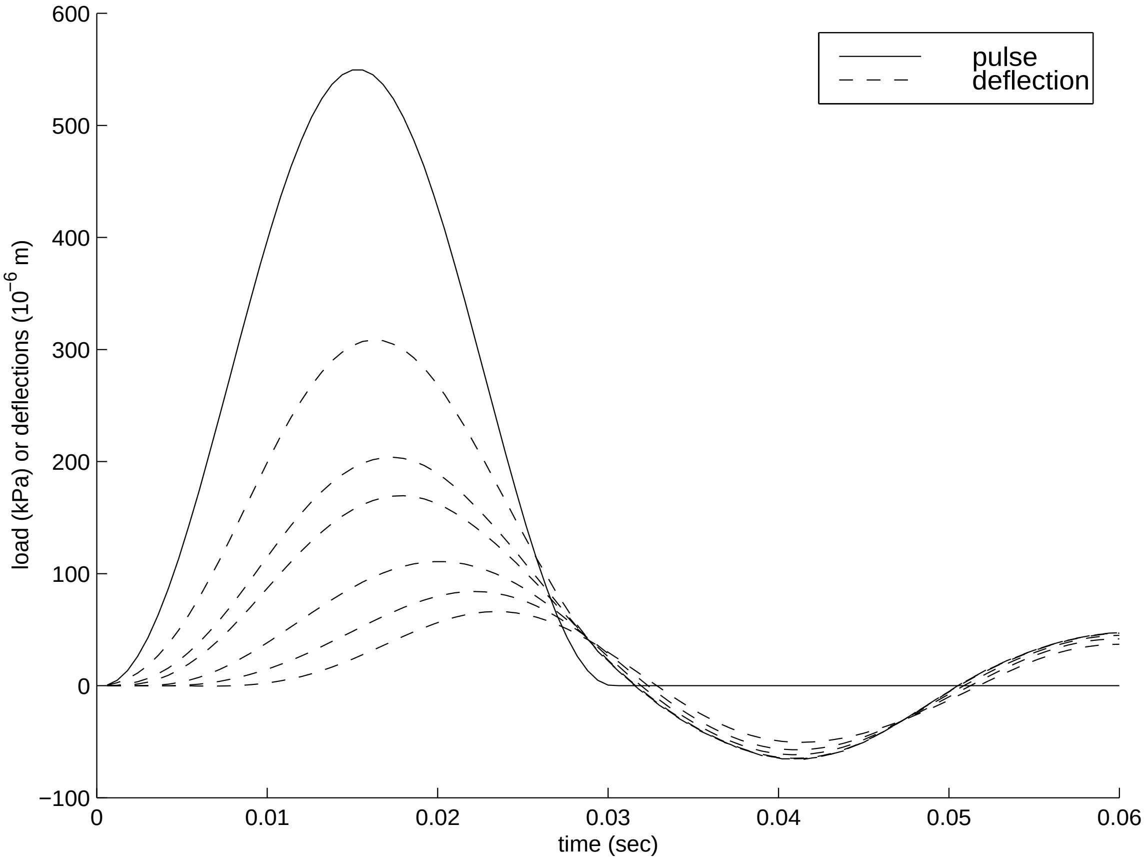

Figure 2.21: Synthesized Data-Typical Pavement

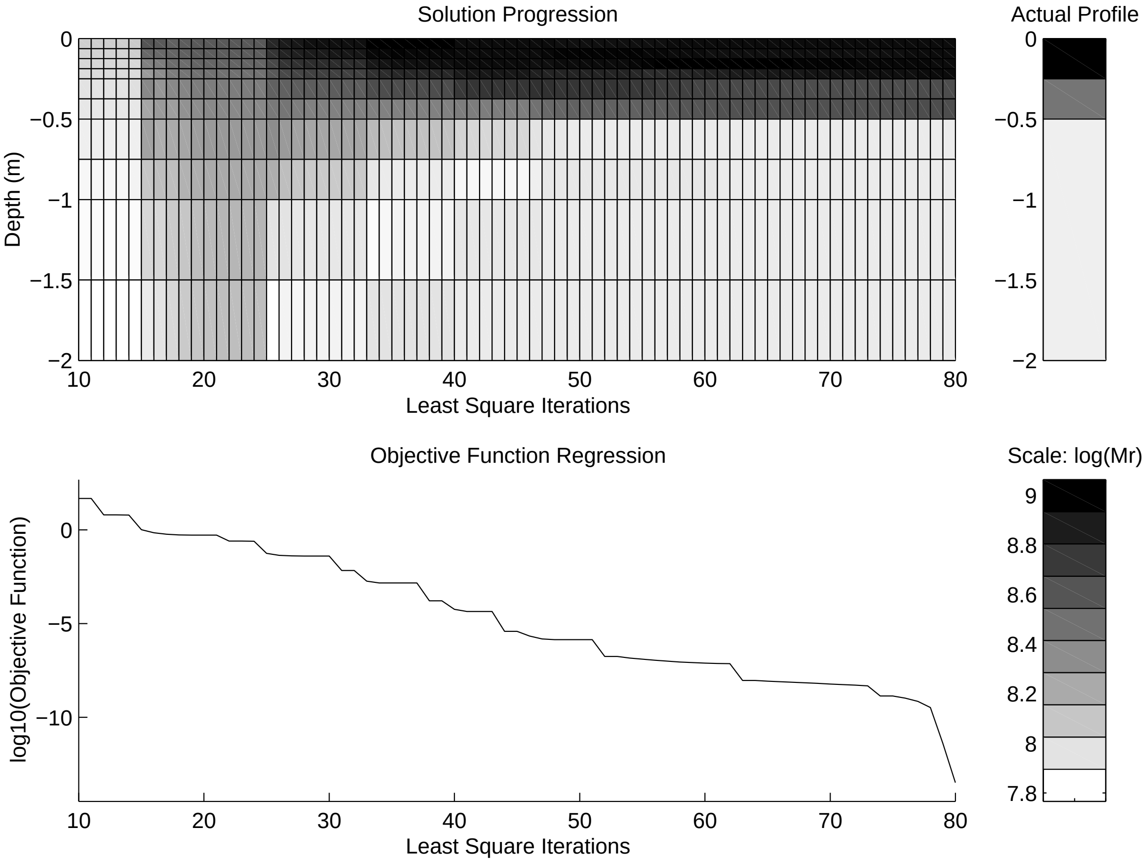

Figure 2.22: Typical 3D Pavement Backcalculation

With this spatial resolution, stiff embedded layers (say, a layer of portland cement concrete covered by asphalt), or thin embedded soft layers (which can represent highly deteriorated subsurface layers or voids) could not be correctly captured. Higher resolutions (for the forward elastodynamic simulation, and for the discretization used in the optimization problem) are necessary to capture these features. Unfortunately, higher resolutions require significantly more computing time and are not practical yet.

### 2.5.3 Field Data

A reconstruction from field data, on a three-layer profile, is illustrated below. In order to perform these computations however, the raw data had to be preprocessed to filter out high frequency noise (anything above 100 Hz) in deflection and pulse data, and correct for a time lag between pulse/deflection that appears in the collected FWD data. In addition, a smaller window of the data was used: the time histories starting at pulse initiation, and a few data points after pulse end were included in the backcalculation. Using the full window would require additional data correction (as has been proposed in the past [21]), and was not deemed necessary since the time window used contained most of the information needed. The raw and corrected data used in the backcalculation are shown below in Figures 2.23 and 2.24 respectively.

Reconstruction results are shown in Figure 2.25. Only the top one meter of pavement stiffnesses are plotted (a thick 8m layer exists at the bottom of the model to simulate an ”infinite” depth to bedrock). Final stiffness results were: $\{1.529e9, 1.179e9, 7.255e8, 3.955e8, 2.095e8,$ $1.199e8, 7.752e7,$ $6.324e7, 6.200e7,$ $8.084e7,$ $1.056e8, 1.056e8\}$. The objective function values approached $10^{-2}$, and a pattern with a stiff upper layer and a softer lower layer did develop. Note that the discretization used in this backcalculation did not take advantage a-priori information about layer depths, and therefore the reconstruction has computational layers that span physical layer boundaries. A finer resolution will naturally capture these boundaries better.

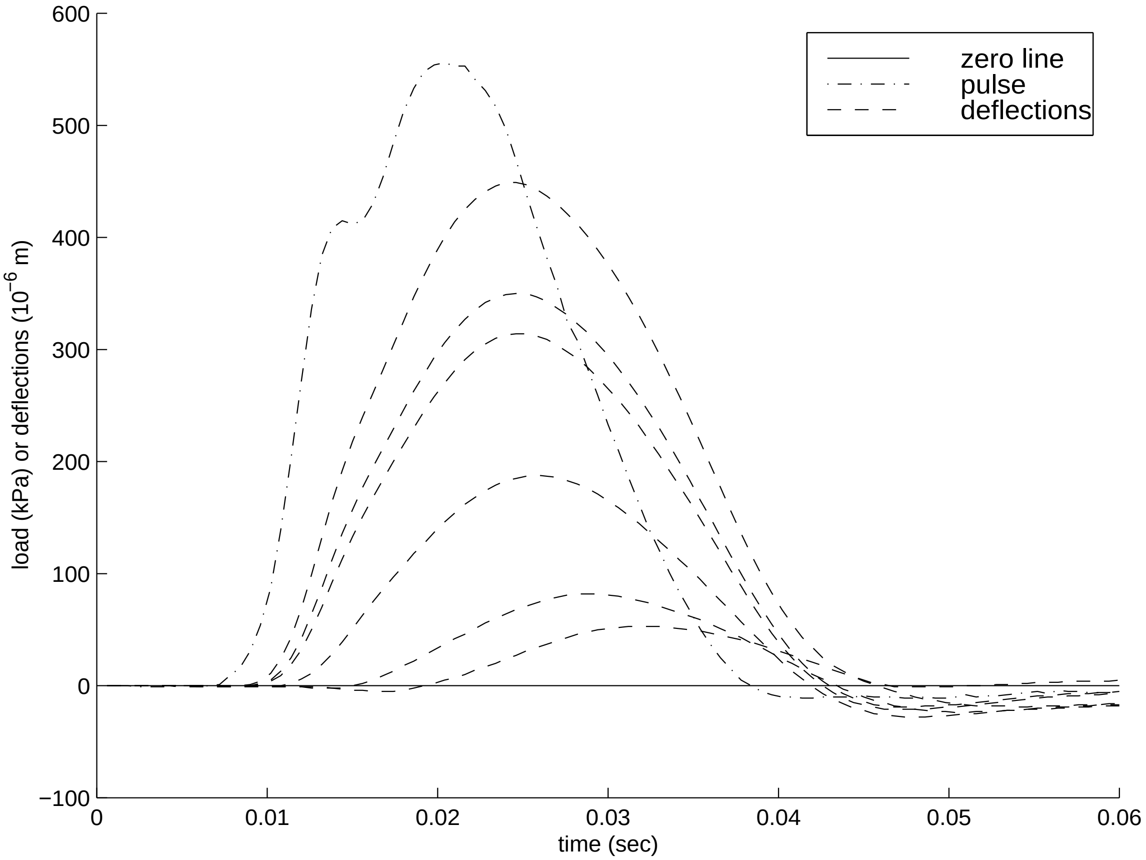

Figure 2.23: Raw FWD Data

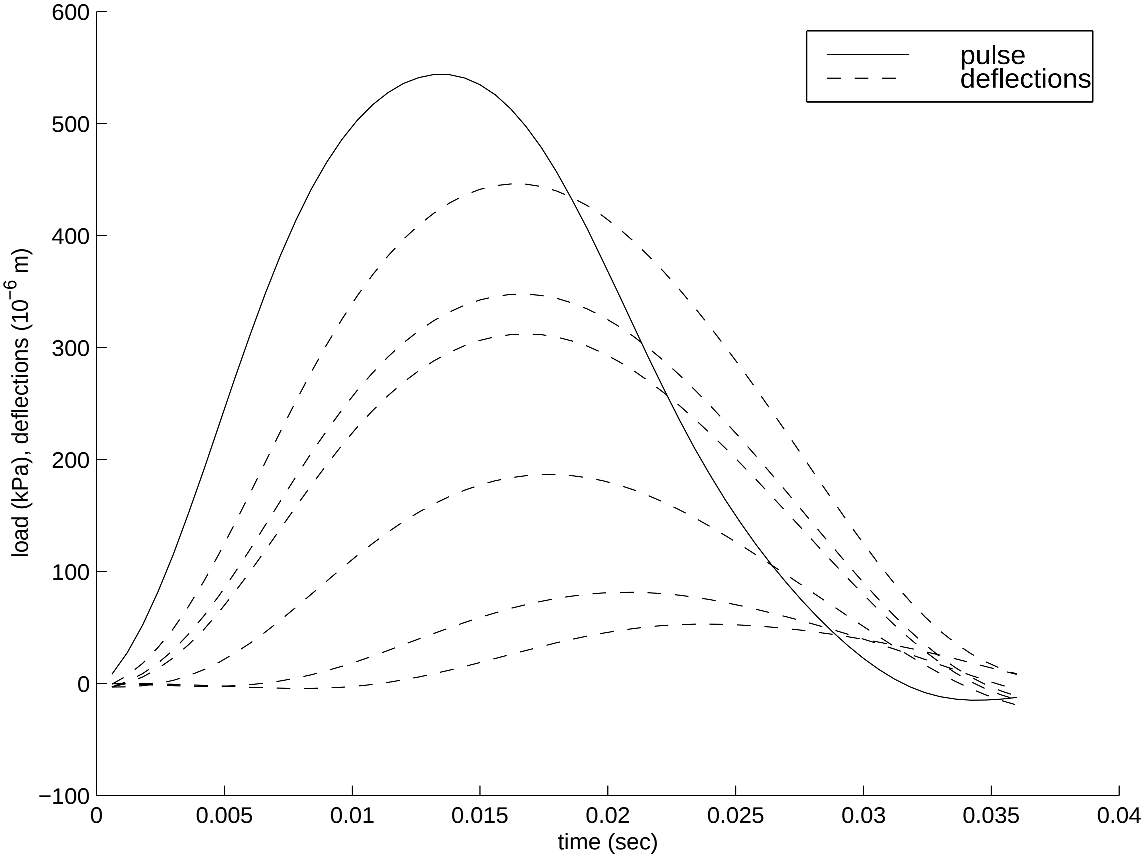

Figure 2.24: Processed Backcalculation Data

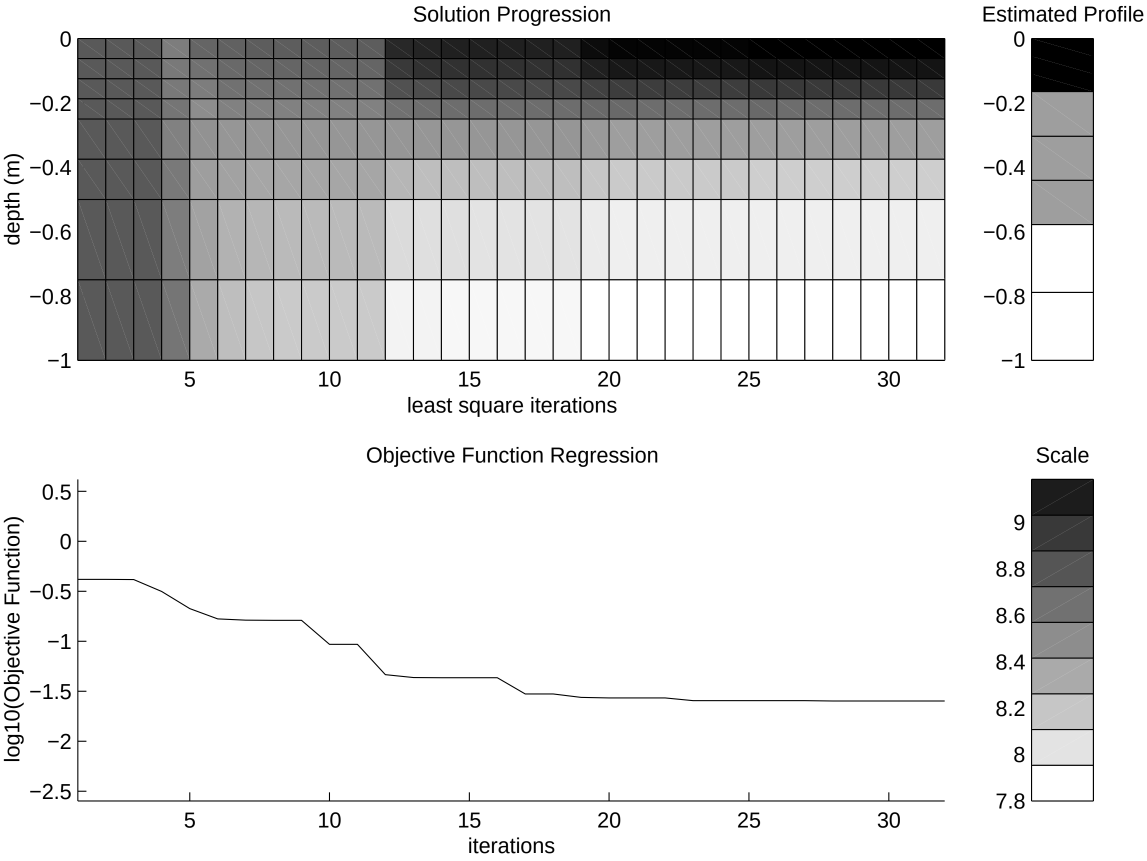

Figure 2.25: Results with nonconforming Mesh

# Chapter 3

# Efficient Methods for the Forward Problem

The main computational bottleneck for the backcalculation procedure described in the previous chapter is the forward simulation: the three dimensional elastodynamic problem whose solution is needed at every iteration of the optimization procedure. It is therefore essential to develop methods that can efficiently perform this computation. This chapter summarizes the methods we developed for this purpose.

## 3.1 Formulation in the Interior of the Domain

The basic equations governing wave propagation in continuous media may be written as a hyperbolic system of partial differential equations in 1, 2 or 3 space dimensions. Finite volume methods (FVM) are powerful numerical methods particularly suited for wave propagation problem in heterogeneous media. They rely on discretizing the spatial domain into cells, and solving "Riemann problems" at cell boundaries. Riemann problems involve determining the local wave structure at these boundaries, to propagate waves to neighboring cells in a stable fashion that eliminates numerical oscillations. These methods were originally designed to capture shock waves and can be used with similar effectiveness for linear and nonlinear problems [14].

For an axisymmetric domain, the governing equations may be expressed as:

$$q_t + Aq_r + Bq_z = \psi(q) \tag{3.1.1}$$

Subscripts denote differentiation (with respect to time t, the radial direction r, or the vertical direction z).

$$q = \begin{bmatrix} \sigma_{rr} \\ \sigma_{zz} \\ \sigma_{rz} \\ v_r \\ v_z \end{bmatrix}, A_{3Daxi} = \begin{bmatrix} 0 & 0 & 0 & (\lambda+2\mu)n^r & \lambda n^z \\ 0 & 0 & 0 & \lambda n^r & (\lambda+2\mu)n^z \\ 0 & 0 & 0 & \mu n^z & \mu n^r \\ \frac{n^r}{\rho} & 0 & \frac{n^z}{\rho} & 0 & 0 \\ 0 & \frac{n^z}{\rho} & \frac{n^r}{\rho} & 0 & 0 \end{bmatrix}, \psi(q,\kappa) = \begin{bmatrix} \frac{(\lambda+2\mu)\sigma_{rr}-\lambda\sigma_{zz}}{2\rho(\lambda+\mu)r} \\ \frac{1}{\rho r}\sigma_{rz} \\ 0 \\ 0 \\ 0 \end{bmatrix}$$

$n^r$ and $n^z$ are the radial and vertical components of a unit vector in the direction of propagation. The coefficient matrices A and B may be obtained from $A_{3Daxi}$ by setting the n-direction to the radial and vertical directions. $\psi(q)$ is a ”source” term and $r$ is the distance from the center of the axisymmetric domain. $\sigma_{ij}$ are the components of the stress tensor, and $v$ is the velocity of the medium. $\lambda$ and $\mu$ are the Lamé coefficients for linear elastic materials. They are related to the Young's modulus $E$ and the Poisson's ratio $\nu$.

$$\lambda = \frac{E\nu}{(1+\nu)(1-2\nu)} \tag{3.1.2}$$

$$\mu = G = \frac{E}{2(1+\nu)} \tag{3.1.3}$$

The wavespeeds of the primary and secondary waves $c_p, c_s$, that is waves which oscillate in the direction of the wave propagation and orthogonal may then be expressed in terms of the material coefficients as:

$$c_p = \sqrt{\frac{E}{\rho}} = \sqrt{\frac{\lambda+2\mu}{\rho}} \tag{3.1.4}$$

$$c_s = \sqrt{\frac{\mu}{\rho}} \tag{3.1.5}$$

Note that the wavespeed grows with higher values of $E$. This fact is crucial since it has big implications on the computational cost, as the largest time step that can be used in the solution must satisfy the stability condition:

$$\triangle t \leq \frac{C \cdot \triangle x}{c_p} \tag{3.1.6}$$

where $\triangle x$ is the cell size and $C$ the Courant number ($C \leq 1$). This restriction has a considerable impact on the computation time. For larger stiffness and consequently larger wavespeed $c_p$ the timestep $\triangle t$ decreases and the number of time steps goes up. Equation 3.1.4 shows that if the stiffness increases by a factor of ten the timestep $\triangle t$ decreases and hence the number of steps increases by a factor of $\sqrt{10} = 3.16$. It is also worth noting that a finer spatial discretization $\triangle x$ also requires smaller time steps.

## 3.2 FWD Simulations

The solution of the elastodynamic set of equations by FVM consists of an explicit time integration. At every time step stress and velocity discontinuities at an interface between cells give rise to waves propagating into the adjacent cells, and are used to update the stress and velocities for the next time step. Details of the algorithm and its implementation may be found in [22]. We summarize the main FWD-specific features of the implementation in this section.

### 3.2.1 Graded Discretizations

Cartesian grids are often the most desirable spatial discretizations from a computational perspective. They are efficient, can readily take advantage of the memory hierarchies of modern computer architectures, and require relatively simple data structures for implementation. Using a uniform cartesian grid for the whole simulation domain however is wasteful not only because of the increased number of cells, but also because the necessary reduction of the time step over the whole computational domain.

To take advantage of the efficiency of cartesian grids, without introducing unnecessary spatial refinement everywhere, our discretiation consists of a multi-level grid, where regions in which more accuracy is needed rely on a finer discretization locally. The refined parts of the computational domain are handled as rectangular (superposed) patches as shown in Figure 3.1 (the figure shows half of the axisymmetric formulation). The load, and sensors, are located on the top left part of the grid (refined region). The left boundary is a symmetry boundary. The right and bottom boundaries of the computational grid are absorbing boundaries that allow outgoing waves to go through unreflected into the domain.

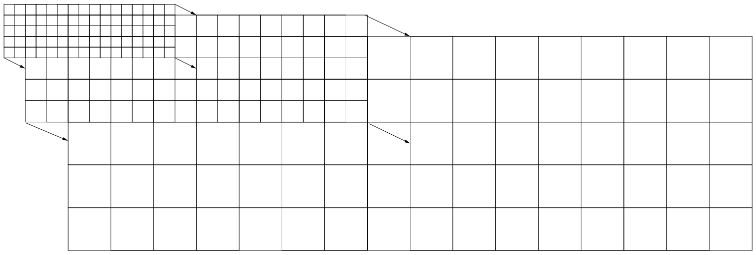

Figure 3.1: Three superposed grid patches. The upper leftmost patch is the most refined.

This multilevel discretization not only allows coarser cells to be used far away from the region where accuracy is most needed, but also allows large time steps to be used in those regions. The largest time step, as mentioned previously, depends on the cell size of the discretization. Standard finite element simulations suffer from the problem that the time step for dynamic simulations must be constant everywhere in the domain, and hence are constrained by the smallest cell size. The methods proposed here allow the natural use of different time steps in different regions of the grid, and therefore result in significant computational speedup. In this work the grid patches for the different refinement levels have the following sizes and are placed according to Figure 3.1 ($l$ and $h$ are domain width and cell size):

- level 3 patch(finest): $l_3 = 1/4 \cdot l$, $h_3 = 1/4 \cdot h$
- level 2 patch: $l_2 = 1/2 \cdot l$, $h_2 = 1/2 \cdot h$
- level 1 patch: $l_1 = l$, $h_1 = h$

### 3.2.2 Symmetry and Absorbing Boundary Conditions

In order to save half of the computational cost symmetry boundary conditions were implemented. At the symmetry boundary we have: $\sigma_{xy} = u = 0$. Figure 3.2 shows how the implementation is handled. Two layers of "ghost cells" are introduced to store the information needed to impose symmetry on the computations performed in the main computational domain.

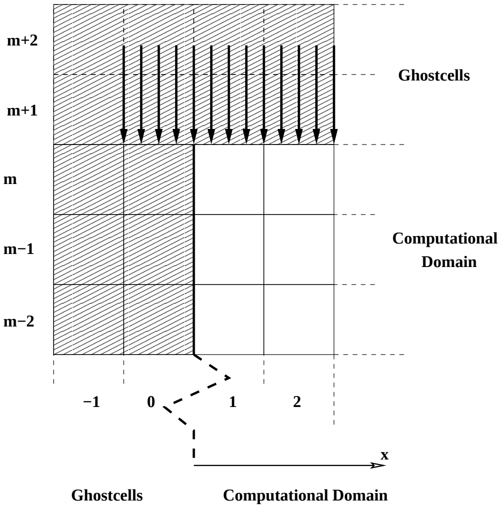

Figure 3.2: Applying the load in the case of the symmetry boundary condition.

In FVM simulations, the computational domain is finite. An infinite physical domain is being truncated at some distance to generate the finite computational grid. It is thus necessary to impose boundary conditions that allow us to compute on the finite smaller domain and obtain results that agree with what would be computed on a larger domain. For wave propagation problems, these boundary conditions are known as "absorbing boundaries". Effective absorbing boundary conditions can be obtained by simply using zero-order extrapolation from the boundaries of the grid to "ghost cells" that are added to the domain. This simple approach to absorbing boundary conditions works remarkably well for one-dimensional as well as multidimensional problems.

The approach used is shown in Figure 3.3. At the boundary, only outgoing waves are supposed to cross the interface between the computational domain and the ghostcells. This approach seems reasonable in the case of FWD tests where the waves propagate away from the place of impact.

Figure 3.3 shows the right boundary of a computational domain. On the left the zero order boundary conditions are shown. The values of $q(x, t)$ are simply transferred from the outmost cell in the domain $(m, j)$ to the ghostcells $(m + 1, j)$, $(m + 2, j)$. This strategy relies on the fact that the Riemann problem at the edge of the computational domain has the same data on either side, resulting in zero-strength waves and in particular no ingoing waves [14] into the computational domain.

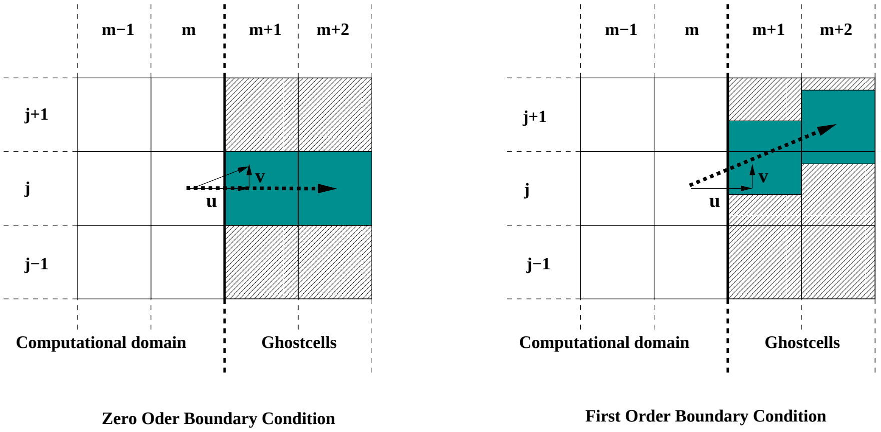

Zero Oder Boundary Condition

First Order Boundary Condition

Figure 3.3: Implementation of zero order boundary conditions (left) and first order boundary condtitions (right).

Zero order extrapolation boundary conditions lose some of their efficiency if the waves do not exit the domain in a perpendicular direction to the boundary. We tested an implementation of first order boundary conditions. See Figure 3.3, right. The direction of the wave propagation is assumed to be identical to the direction of the displacement in the cell $(m, j)$. Therefore the velocities $u, v$ determine the direction in which $q(x, t)$ of the cell $(m, j)$ will be shifted. In Figure 3.3 $q(x, t)$ is split to cells $(m + 1, j), (m + 1, j + 1)$ and $(m + 2, j), (m + 2, j + 1)$ respectively. This approach yields smoother results but does not dissipate enough energy and hence was not used any further.

### 3.2.3 Coordinate mapping

Another mechanism to improve the accuracy of the solution with a limited computational budget, involves coordinate mapping which stretches the spatial grid but still allows the underlying computations to be performed on a uniform and/or multilevel cartesian grid. Mapping is a very useful tool in backcalculations. It allows us to maintain a fixed and uniform/multilevel computational grid to which the data is mapped (see Figure 3.4). Hence meshing flexibility can be achieved and the computational model can be easily adapted to different pavement configurations. Given that the top layers are relatively thin, this allows the use of more computational grid points in these regions.

In this work only mapping in the vertical direction is implemented. Mapping is implemented via a capacity function $\kappa_i$ that is introduced in the discretized equations. $\kappa_i = \triangle x_i / \triangle \xi$, where $\triangle \xi$ is the cellsize of the appropriate grid level (Figure 3.4, left) in the vertical direction and $\triangle x_i$ is the vertical cellsize of the ith layer in the real profile (Figure 3.4, right) which changes over the height of the domain. In the case of a uniform real profile $\kappa_i = 1$ for all cells $i$. Coordinate mapping decreases the contrast in the effective computational wave speeds in various regions of the grid, improving the stability of the forward solver.

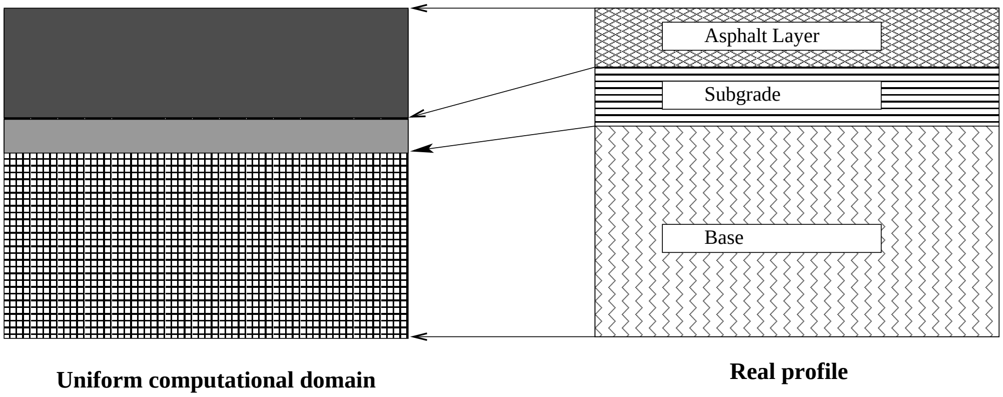

Figure 3.4: Pavement Profile (right) is mapped to the computational domain (left).

We have experimented numerically with the grid parameters described in this chapter (size of the computational domain, location/extent of the vertical and horizontal boundary conditions, time step and number of grid levels in the hierarchy, etc.). Using this implementation, performing a reliable 3D forward simulation for typical moduli, over the time duration of the FWD test (∼ 60ms), requires on the order of 20 min on typical desktop machines (3GHz Pentium) depending on the specific profile. A multi-processor prototype implementation has been done [22] and is currently being tested and refined to improve its runtime. Since the backcalculation procedure typically requires dozens of calls to the forward problem, the importance of speeding up the forward problem can not be understated.

# Chapter 4

# Conclusions

The goal of this study was to evaluate the ability to recover pavement layer modulii and thicknesses from dynamic Falling Weight Deflectometer data.

- The vertical profile is discretized into a number of ”thin computational layers”, and the modulii of these layers are used as the variables in an optimization problem that seeks to minimize the residual error between computed and observed time history data. Physical layer thicknesses may be obtained, post-optimization, by grouping thin layers of similar properties. A gradient in modulii within a physical layer may also be captured in this fashion.

- The basic optimization problem, a nonlinear least squares problem, is ill-posed. It generally fails to converge, even when starting with initial guesses that are ”fairly close”. Numerically, the problem has multiple local minima, as well as regions with flat (and noisy) gradients that can send the iterative numerical solution far away from the true optimum.

- Regularization terms that control the change in the layer modulii must be added to the residual objective function to avoid convergence problems. Two regularization terms have been identified and tested for the FWD backcalculation problem. One involves the absolute values of the modulii to prevent physically-unrealistic solutions with large layer modulii. The other controls the gradient of the modulii in the vertical direction to prevent ”rough” solutions, where the optimization converges to a profile consisting of neighboring layers that alternate between stiff and soft.

- Continuation methods are necessary to properly implement the regularized minimization problem. The weights given to the regularizing terms cannot be generally determined a-priori. A continuation scheme for slowly reducing the weights on these terms provides an effective computational strategy for implementing the regularized minimization.

- Noise in the data can be managed with the continuation scheme. Some noise effects can be pre-processed before backcalculation (filtering out high frequency response components, correcting for initial recording lag in the data, etc.). Any remaining noise has to be included in the backcalculation method. Termination criteria must be carefully monitored, so that the backcalculation continues only as long as when the residual norm decreases without increasing the regularization terms. Large values of the regularizing terms indicate physically unrealizable profiles.

- The solution of the forward problem (and its adjoint for computing derivatives of the objective function) remains a critical bottleneck from a computational perspective. Given that the calls to the forward problem occur in the inner loop of the optimization problem, and therefore is run repeatedly during solution, it is important to develop computationally efficient methods for the elastodynamic problem. Multiprocessor machines may be necessary to generate solutions in a reasonable time frame for office use.

Additional work to overcome some of the current limitations include:

- A fast parallel implementation of the forward problem. As mentioned above, a parallel implementation of the forward solver has been developed and can provide significant speedup (since it uses multi level cartesian grids with data structures that can be parallelized effectively). Another improvement on the forward problem could include a hybrid solution scheme where a finite volume discretization in the immediate region in the vicinity of the loading plate and geophones is used, coupled with a layered elastic solution in the deeper far-away region.
- A better tuning of the termination criteria for weighing the balance between minimizing the residual and the regularizing terms. This will require more numerical experimentation with field data to study the effect of noise on the convergence of the solution. Use of available a-priori information on the profile may also be used to improve the regularization of the optimization problem.
- A study of the effect of more general material models on the backcalculated profiles. There is some evidence that material properties may be anisotropic and/or the granular base layers have nonlinear stress dependence[10] . Hence the assumptions of isotropic and horizontally uniform layers are not appropriate. The computational infrastructure developed here allows us to consider these generalizations [22] but a comprehensive study requires the implementation of a faster forward solver first.

# Bibliography

[1] Akram, T., Scullion, T., and Smith, R.E., “Comparing Laboratory and Backcalculated Layer Moduli on Instrumented Pavement Sections”, *Nondestructive Testing of Pavements and Backcalculation of Moduli (Second Volume), ASTM STP 1198,* Harold L. Von Quintus, Albert J. Bush, III, and Gilbert Y. Baladi, Eds., American Society for Testing and Materials, Philadelphia, 1994, pp. 170-202.

[2] Anderson, M., “A Data Base method for Backcalculation of Composite Pavement Layer Moduli” *Nondestructive Testing of Pavements and Backcalculation of Moduli, ASTM STP 1026*, A.J. Bush and G.Y. Baladi, Eds., American Society for Testing and Materials, Philadelphia, 1989, pp.201-216.

[3] B. Choubane and R. L. McNamara. A practical approach to predicting subgrade moduli using falling weight deflectometer (FWD) data, Florida Dept. of Transportation, 2000.

[4] Boddapati, K.M., and Nazarian, S., “Effects of Pavement-Falling Weight Deflectometer Interaction on Measured Pavement Response”, *Nondestructive Testing of Pavements and Backcalculation of Moduli (Second Volume), ASTM STP 1198,* Harold L. Von Quintus, Albert J. Bush, III, and Gilbert Y. Baladi, Eds., American Society for Testing and Materials, Philadelphia, 1994, pp. 326-339.

[5] Bube, Kenneth P., Langan, Robert T., “A Continuation Approach to Regularization for Traveltime Tomography”, *64th Annual International SEG Meeting,* Society of Exploration Geophysicists, October 23-28, 1994, Tulsa, Oklahoma, pp. 980-983.

[6] Chou, Y.J., Uzan, J., and Lytton, R.L., “Backcalculation of Layer Moduli from Nondestructive Pavement Deflection Data Using the Expert System Approach”, *Nondestructive Testing of Pavements and Backcalculation of Moduli, ASTM STP 1026*, A.J. Bush and G.Y. Baladi, Eds., American Society for Testing and Materials, Philadelphia, 1989, pp.341-354.

[7] Drnevich, V.P., Hossain, M.M., Wang, J., and Graves, R.C., “Determination of Layer Moduli in Pavement Systems by Nondestructive Testing”, *Transporation Research Record 1278*, TRB, National Research Council, Washington D.C., 1990, pp. 18-26.

[8] Hansen, Per Christian, “*Regularization Tools: A Matlab package for analysis and solution of discrete ill-posed problems”*, *Numerical Algorithms* Vol. 6, J.C. Baltzer AG, Basel, Switzerland, 1994, pp 1-35.

[9] Hansen, Per Christian, "The Use of the L-Curve in the Regularization of Discrete Ill-Posed Problems", *SIAM Journal of Science and Computing* Vol. 14, No.6, November, 1993, pp. 1487-1503.

[10] K. D. Hjelmstad and E. Taciroglu. Analysis and Implementation of resilient modulus models of response of granular solids, ASCE, Journal of Engineering Mechanics, 126, 8, pp. 821-830, 2000.

[11] Irwin, L.H., Yang, W.S., and Stufstad, R.N., "Deflection Reading Accuracy and Layer Thickness Accuracy in Backcalculation of Pavement Layer Moduli", *Nondestructive Testing of Pavements and Backcalculation of Moduli, ASTM STP 1026*, A.J. Bush and G.Y. Baladi, Eds., American Society for Testing and Materials, Philadelphia, 1989, pp.229-244.

[12] E. Kausel and J. M. Roësset. Stiffness Matrices for Layered Soils, Bulletin of the Seismological Society of America, Vol. 71, No. 6, pp. 1743-1761, 1981.

[13] H. J. E. Larsen and Dr. P. Ullditz, Development of improved mechanistic deterioration models for flexible pavements, Danish Road Istitute, Report 89, 1998.

[14] R. J. LeVeque, Finite Volume Methods for Hyperbolic Problems, Camebridge University Press, August, 2002.

[15] U.S. Department of Transportation Federal Highway Administration, National Highway Institute Course No. 13127 Pavement Deflection Analysis Participant Workbook, Publication No. FHWA-HI-94-021, February, 1994.

[16] TRB Committee A2B05; Nonlinear Pavement Analysis Project; http://www.clrp.cornell.edu/A2B05, 2001.

[17] Newcomb, D.E., Van Deusen, D.A., Jiang, Y., Mahoney, J.P., "Considerations of Saturated Soil Conditions in Backcalculation of Pavement Layer Moduli", *Transporation Research Record 1473*, TRB, National Research Council, Washington D.C., 1995, pp. 63-71.

[18] Soroos, E., *Feasibility of Backcalculating Pavement Parameters using FWD Time History Data*, University of Washington M.S. Thesis, 1997.

[19] Thuma, Richard, *Green's Function Analysis of Pavement Deflections due to Moving Wheel Loads,* University of Washington M.S. Thesis, December, 1995.

[20] Ullidtz, P., Coetzee, N.F., "Analytical Procedures in Nondestructive Testing Pavement and Evaluation", *Transporation Research Record 1482*, TRB, National Research Council, Washington D.C., 1995, pp. 61-66.

[21] Uzan, Jacob "Dynamic Linear Back Calculation of Pavement Material Parameters" *Journal of Transportation Engineering*, ASCE, Vol. 120, No. 1, January/February, 1994, pp.109-126.

[22] Honyu Wu. Parallel Methods for Static and Dynamic Simulation of Flexible Pavement Systems, PhD thesis, Dept. of Civ. Engrg., University of Washington, 2002.